

1 Supplementary Figures

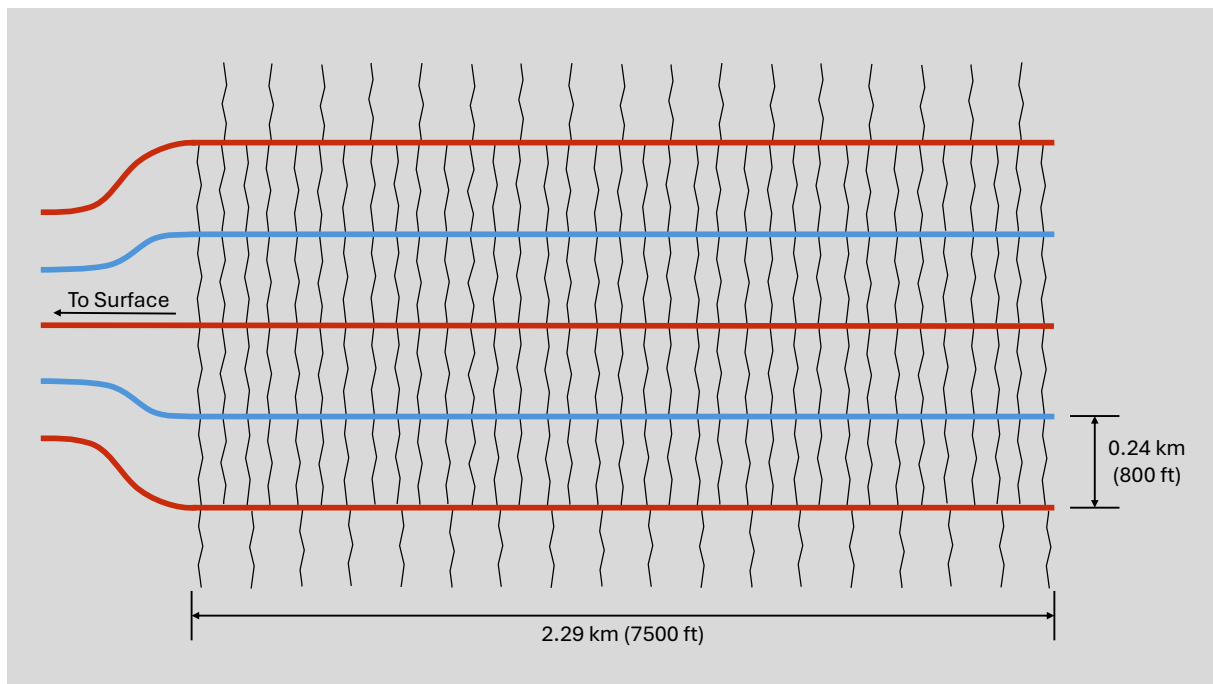


Figure S1: Top-down schematic of the near-term commercial EGS reservoir design used in this work. Injection wells are shown in blue and production wells in red. Individual fractures are drawn for illustrative purposes and do not reflect simulated or expected real world fracture geometries.

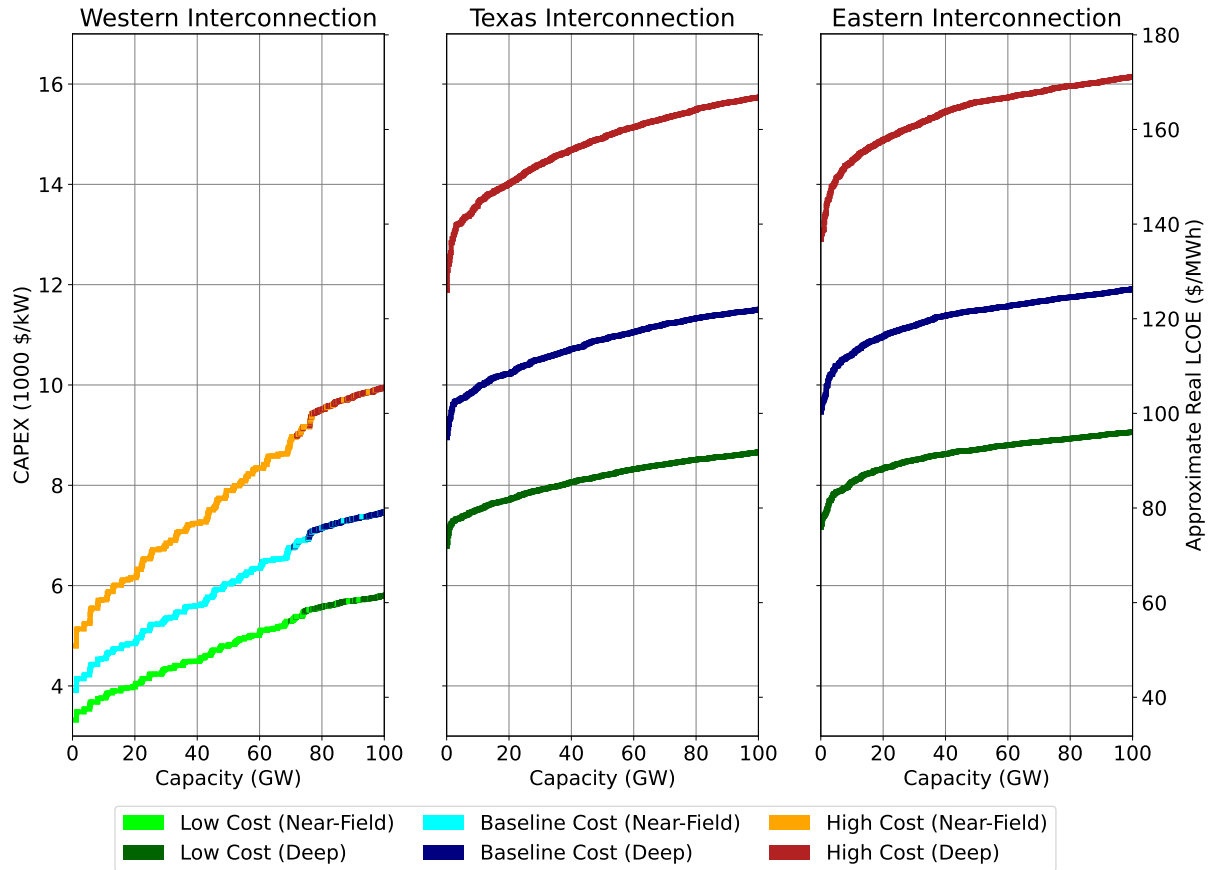


Figure S2: Same as Figure 1 in the main paper, for resources with reservoir temperatures in the 150-350°C range. A higher temperature threshold enables more extensive exploitation of high-quality near-field resources.

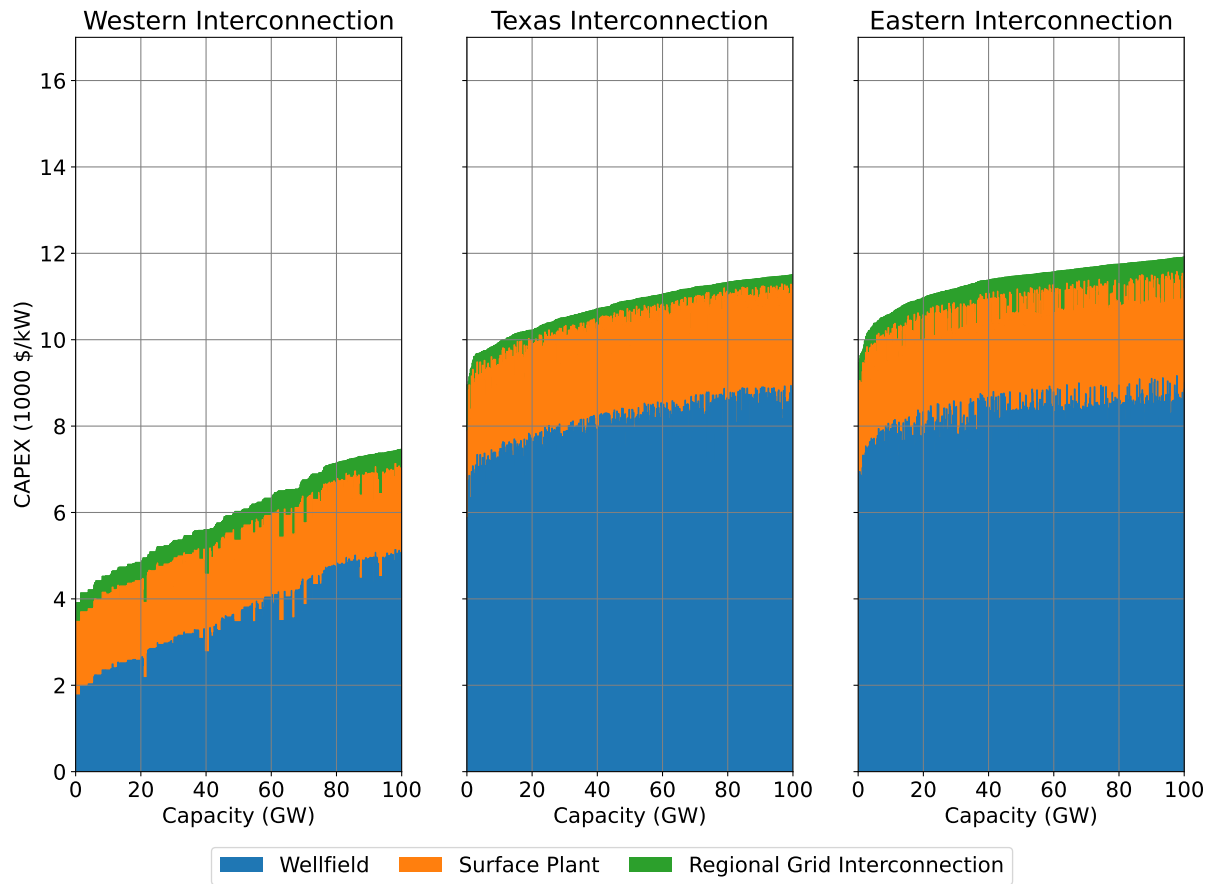


Figure S3: Breakdown of near-term unsubsidized EGS CAPEX by cost component, for the base-line cost case supply curve shown in Figure 1 in the main paper. The wellfield is the largest cost component in most cases. Some otherwise high-quality resources are made more expensive by high interconnection costs.

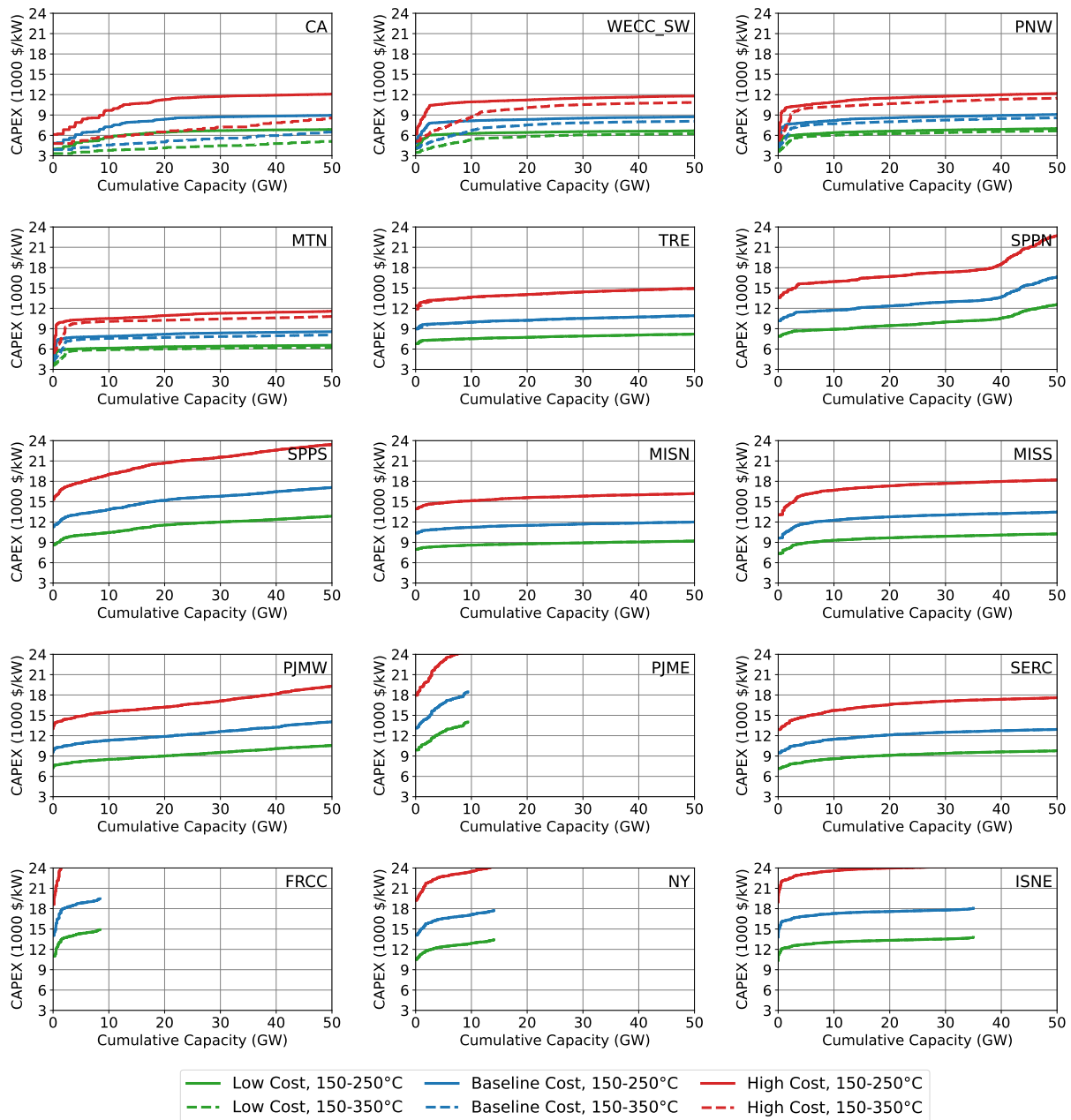


Figure S4: EGS supply curves for 15 US grid regions used in electricity sector capacity expansion modeling in this work (see Figure SS10), for resources in the 150-250°C and 150-350°C ranges, under three different wellfield cost scenarios.

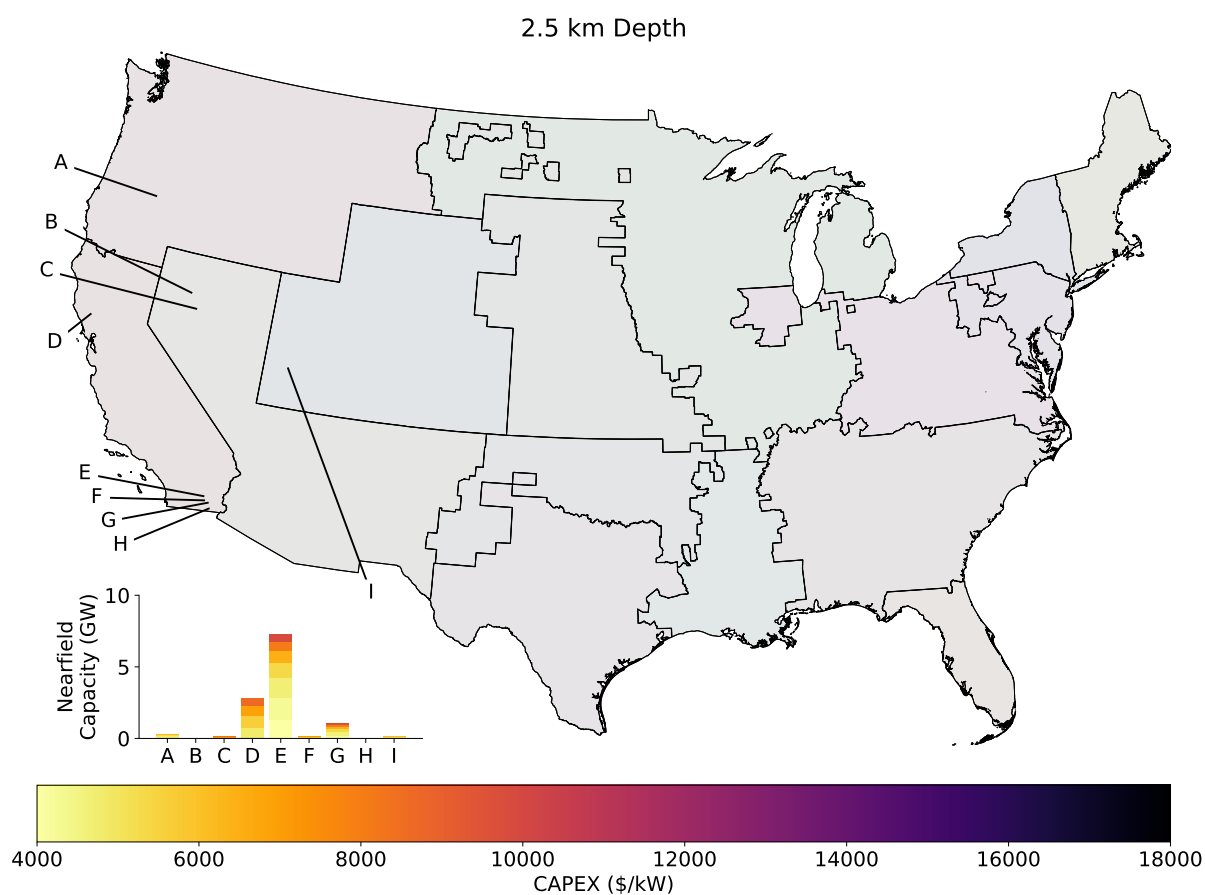


Figure S5: Map showing CAPEX for developable EGS capacity near nine large hydrothermal systems in the western US at a depth of 2.5 km, for reservoir temperatures in the 150-350°C range, under baseline cost assumptions. Grid regions used in electricity sector capacity expansion modeling are also shown.

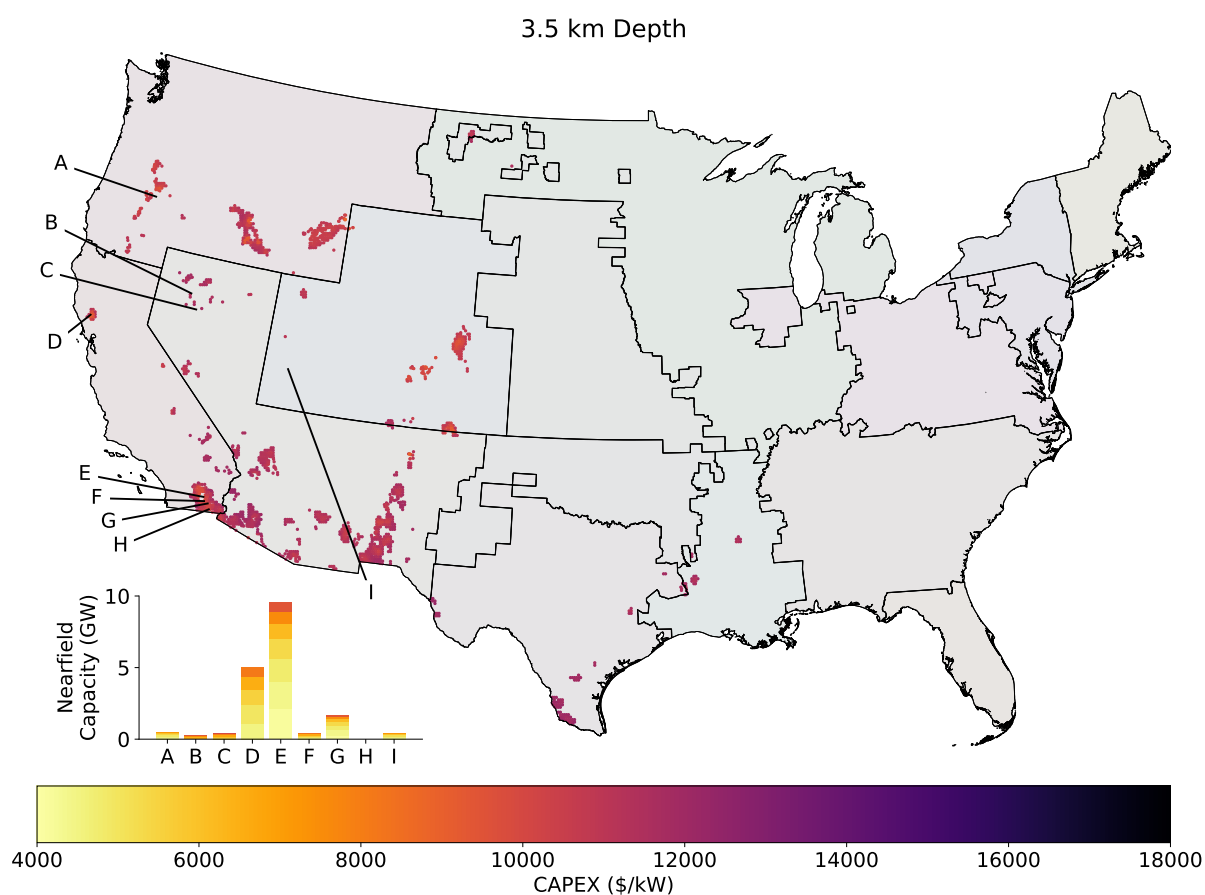


Figure S6: Map showing CAPEX for developable EGS capacity near nine large hydrothermal systems in the western US and at deep EGS candidate project areas nationwide (using temperature-at-depth data sourced from Blackwell et al.¹) at a depth of 3.5 km, for reservoir temperatures in the 150-350°C range, under baseline cost assumptions. Grid regions used in electricity sector capacity expansion modeling are also shown.

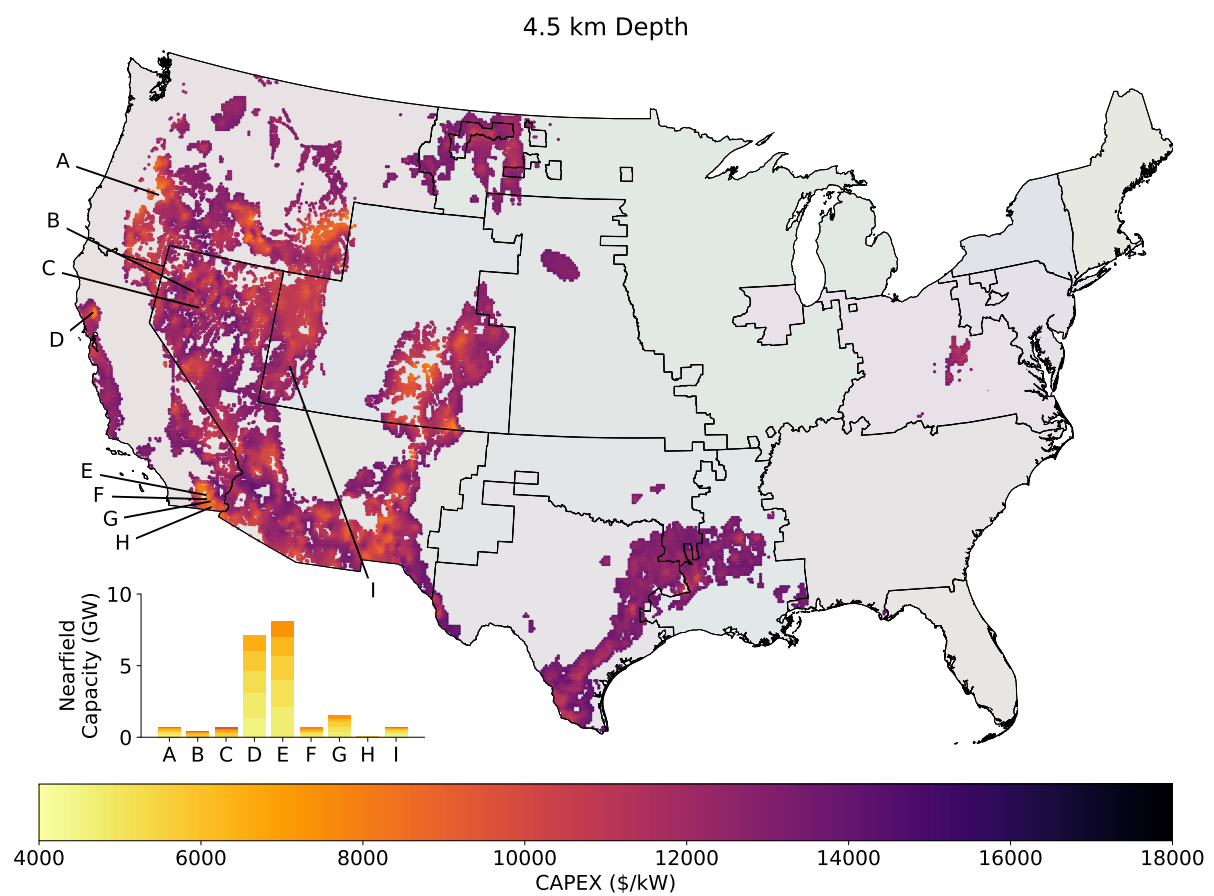


Figure S7: Same as Figure SS6, for resources at a depth of 4.5 km.

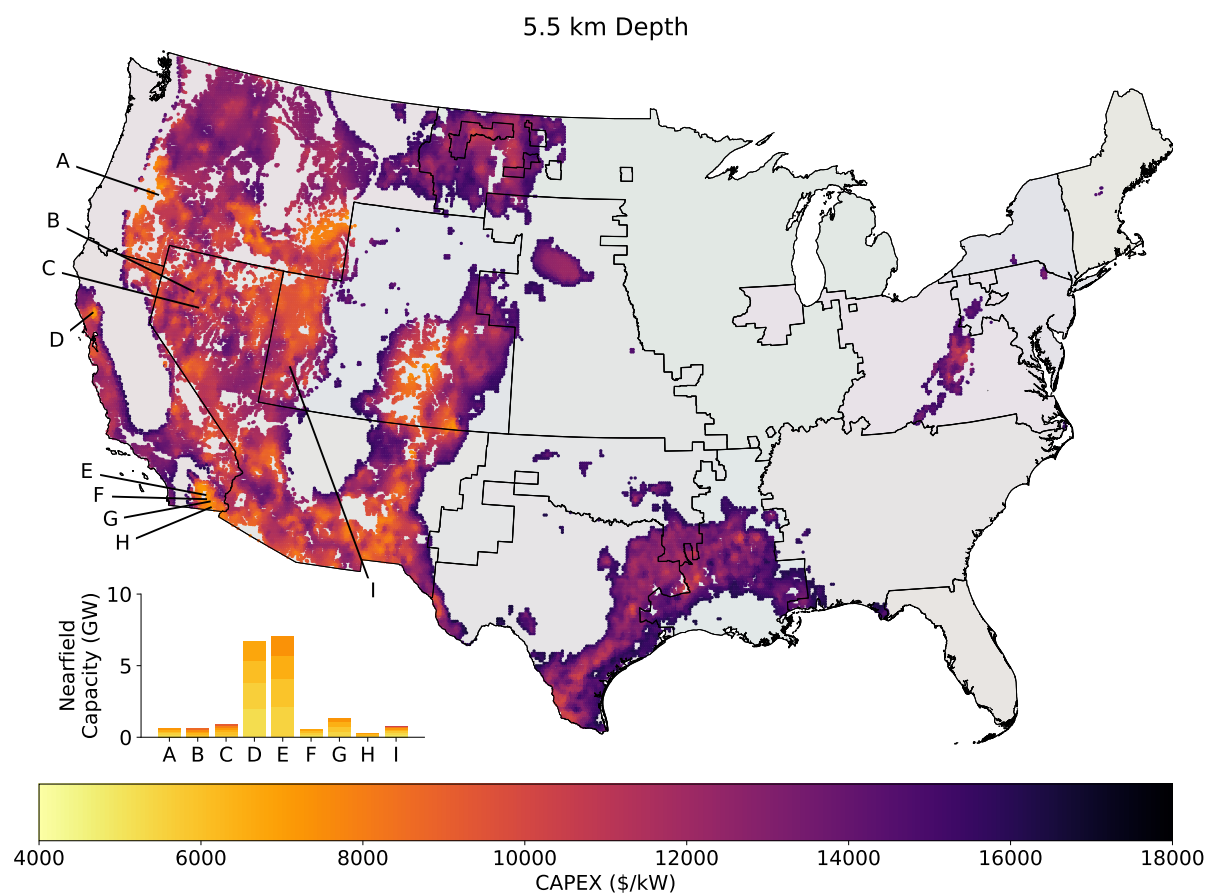


Figure S8: Same as Figure SS6, for resources at a depth of 5.5 km.

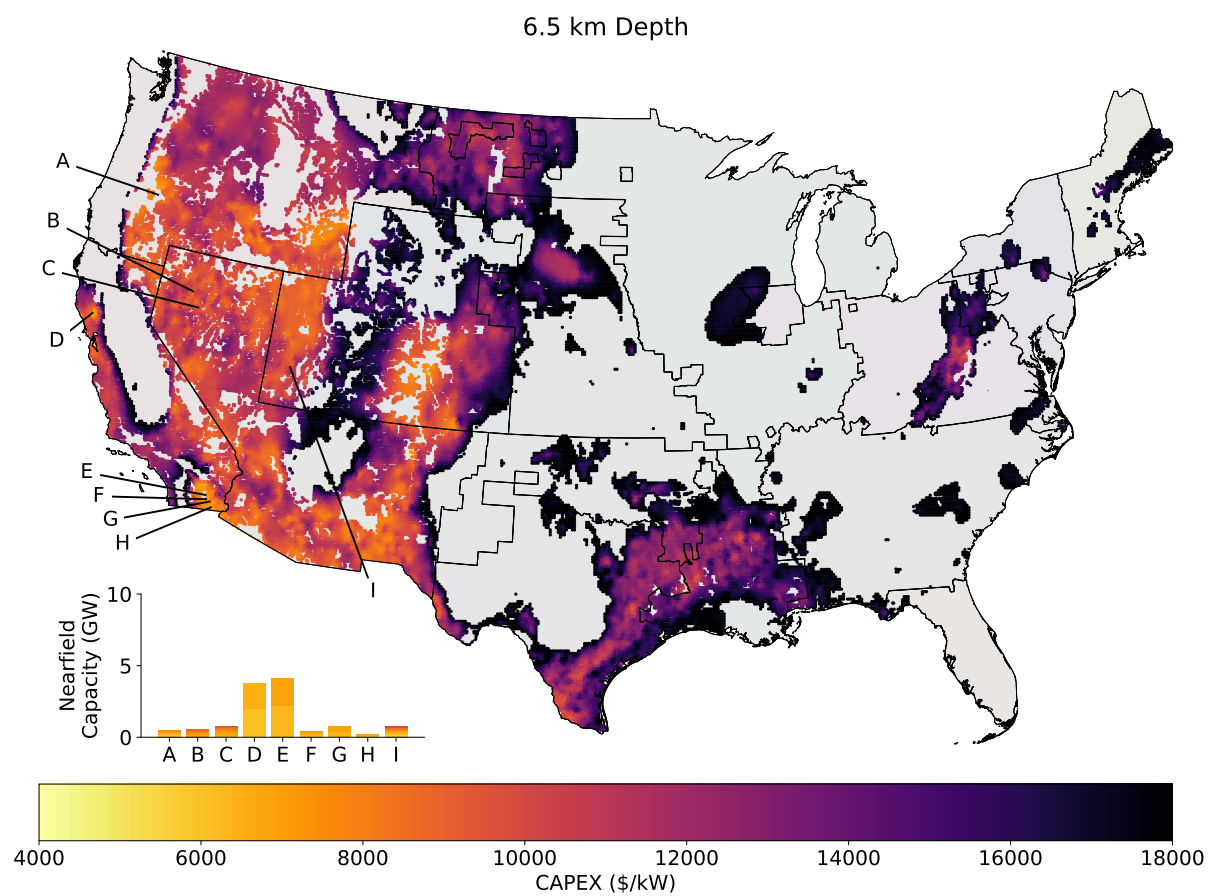


Figure S9: Same as Figure SS6, for resources at a depth of 6.5 km.

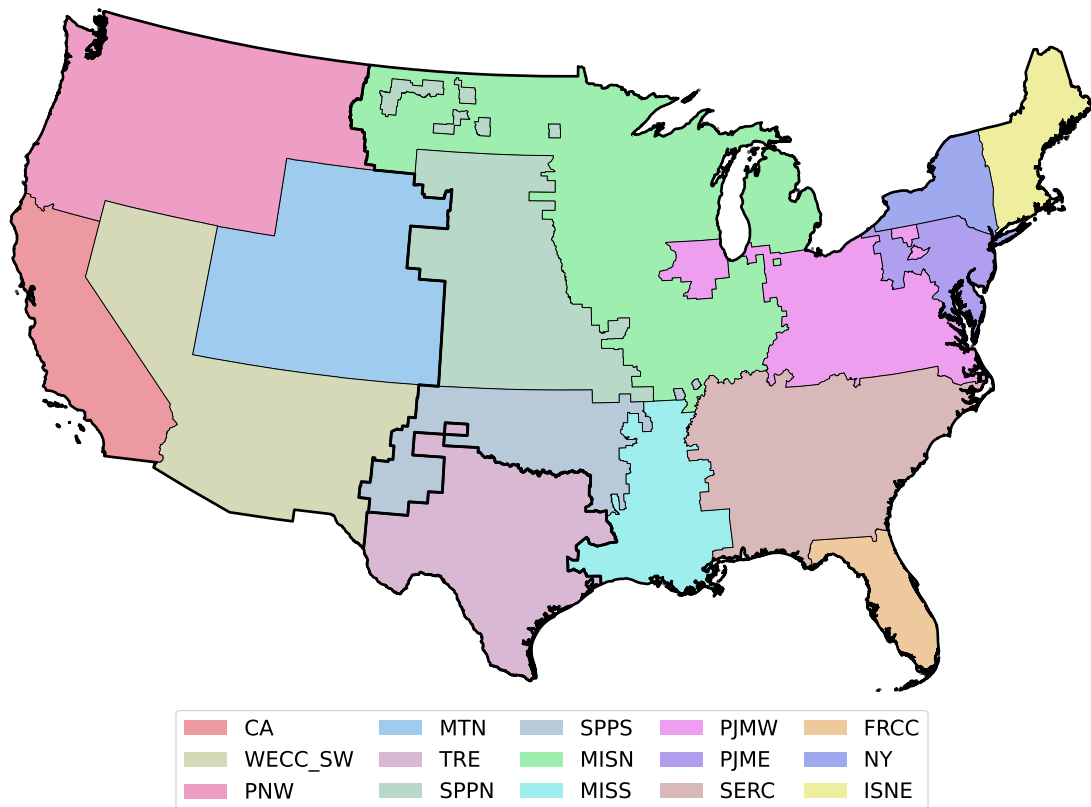


Figure S10: 15-zone topology used to represent the regional structure of the contiguous US electricity system within the GenX electricity system capacity expansion model. Zones are aggregated to minimize internal transmission bottlenecks. The three major synchronous interconnections that make up the US grid are outlined in bold.

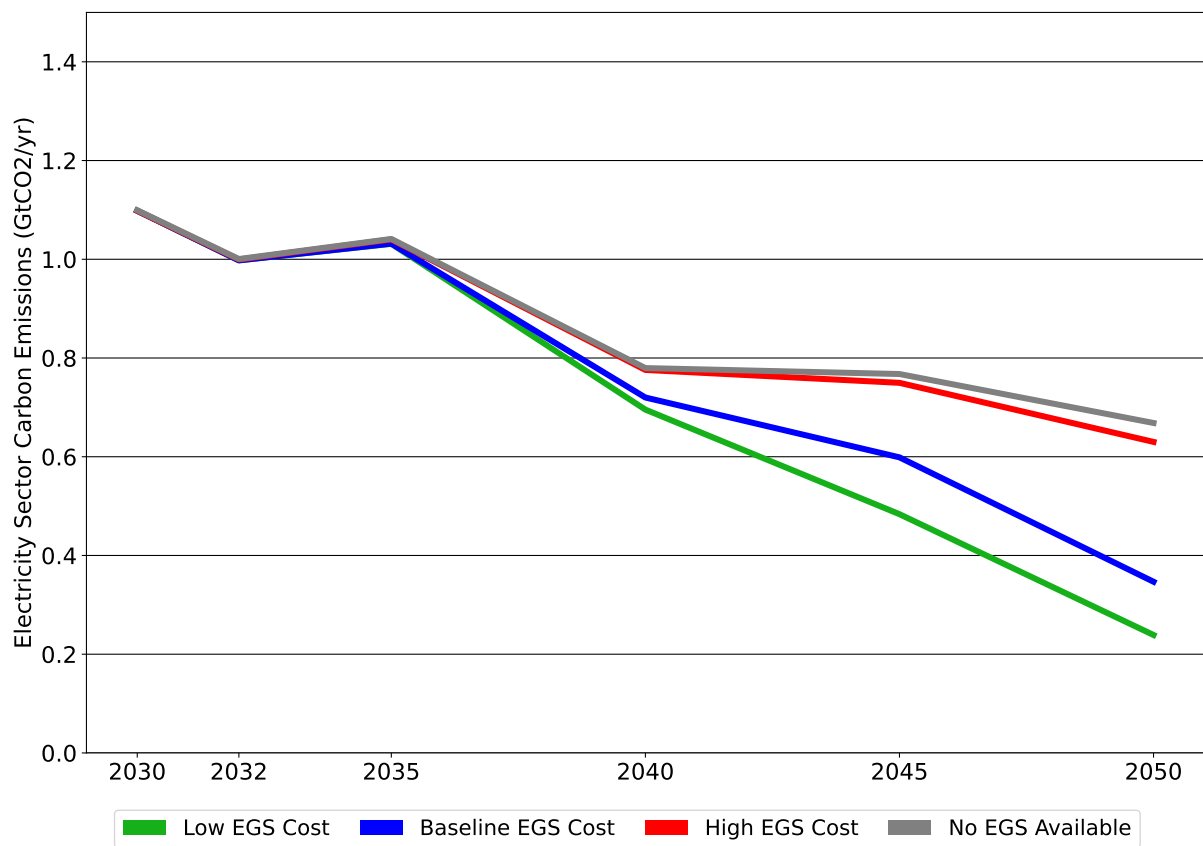


Figure S11: Trajectories of contiguous US power sector CO₂ emissions for three EGS cost cases, and a case where EGS is unavailable, under a current policy scenario.

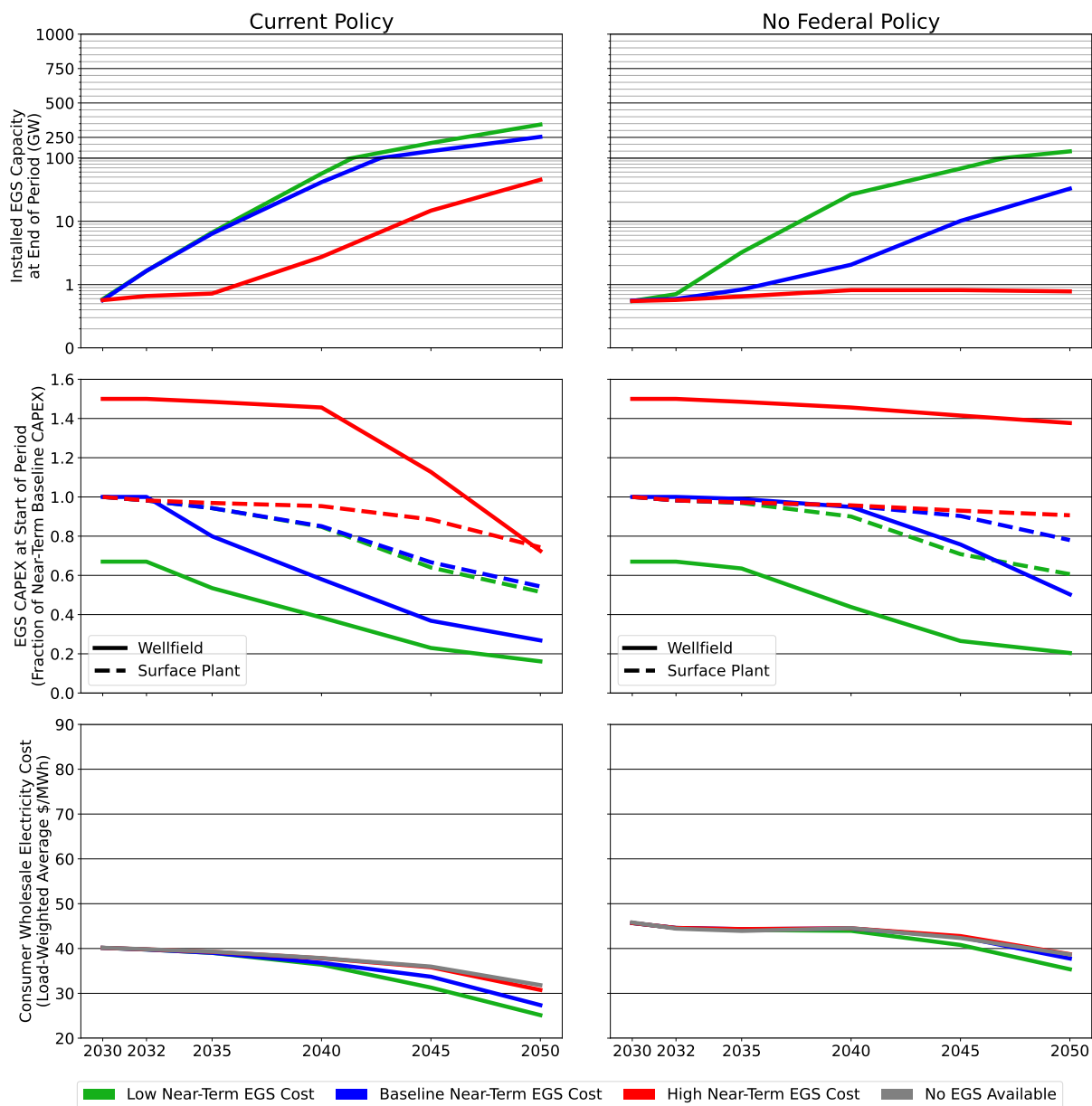


Figure S12: Same as Figure 2 in the main paper, with the “Net-Zero Policy” scenario replaced with a “No Federal Policy” scenario in which all provisions of the 2022 Inflation Reduction Act are rolled back.

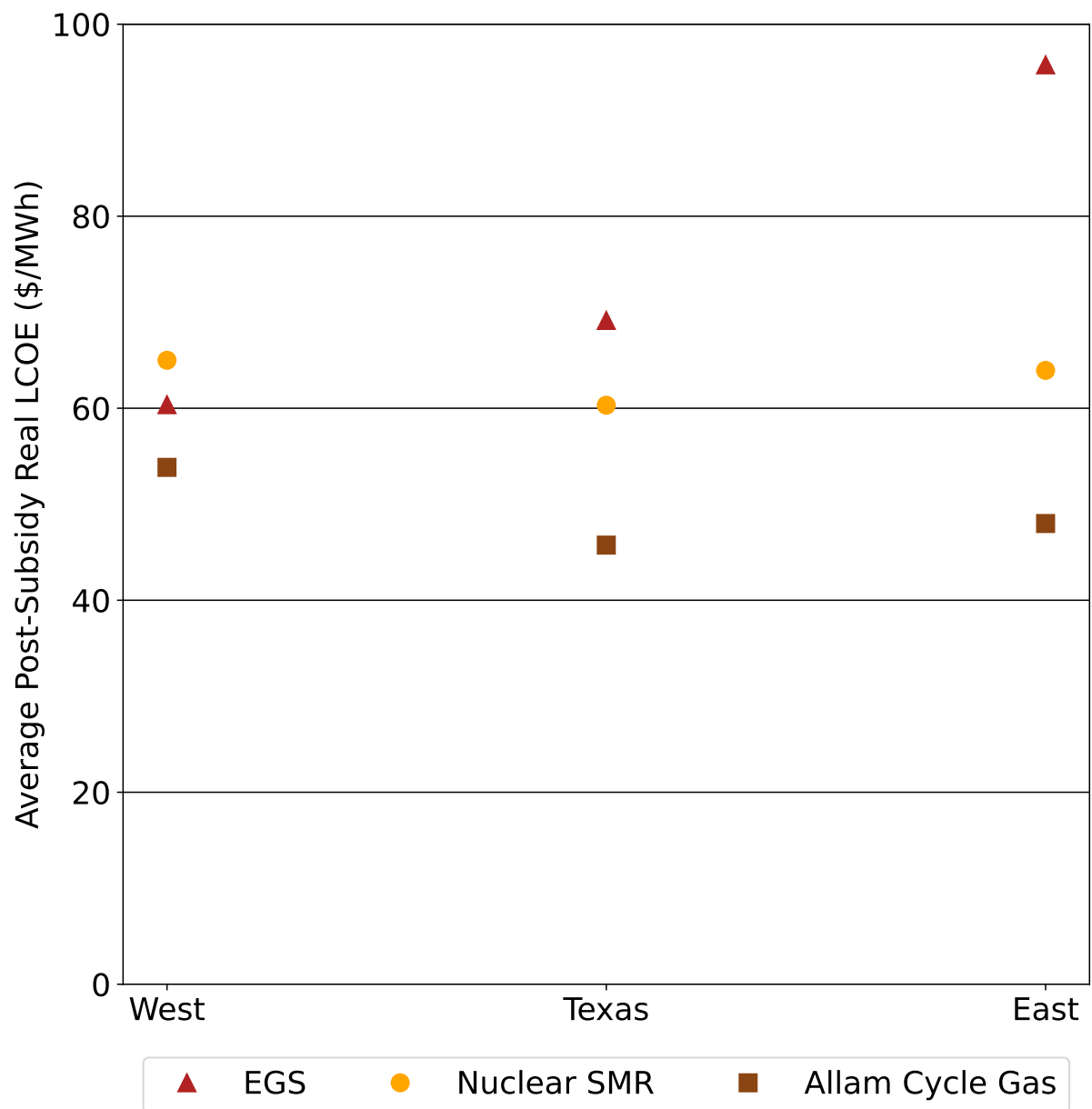


Figure S13: Average post-subsidy real LCOE for EGS at baseline costs (among all sites available for deployment in the model), nuclear SMRs, and Allam cycle gas power plants in the 2031-2032 planning period, for the three synchronous grids serving the contiguous US.

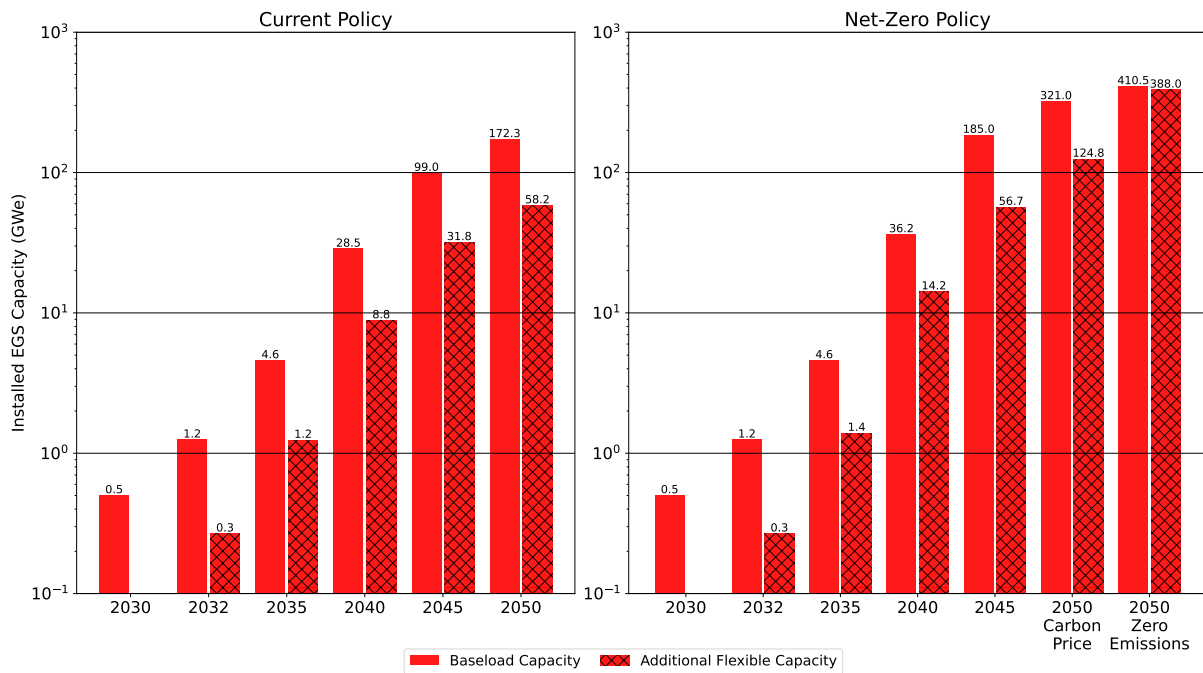


Figure S14: Nationwide installed EGS baseload capacity (the capacity at which the wellfield can produce power at a constant rate under design point conditions while maintaining the target thermal decline rate) and additional flexible capacity (used to enable greater power production for limited durations) for the same scenarios shown in Figures 3 and 4 in the main paper. Note that the sum of baseload and flexible capacities in this figure is not equal to the maximum interconnection capacity shown in Figure 3, as low ambient air temperatures can cause the power plant to generate above its rated design point capacity.

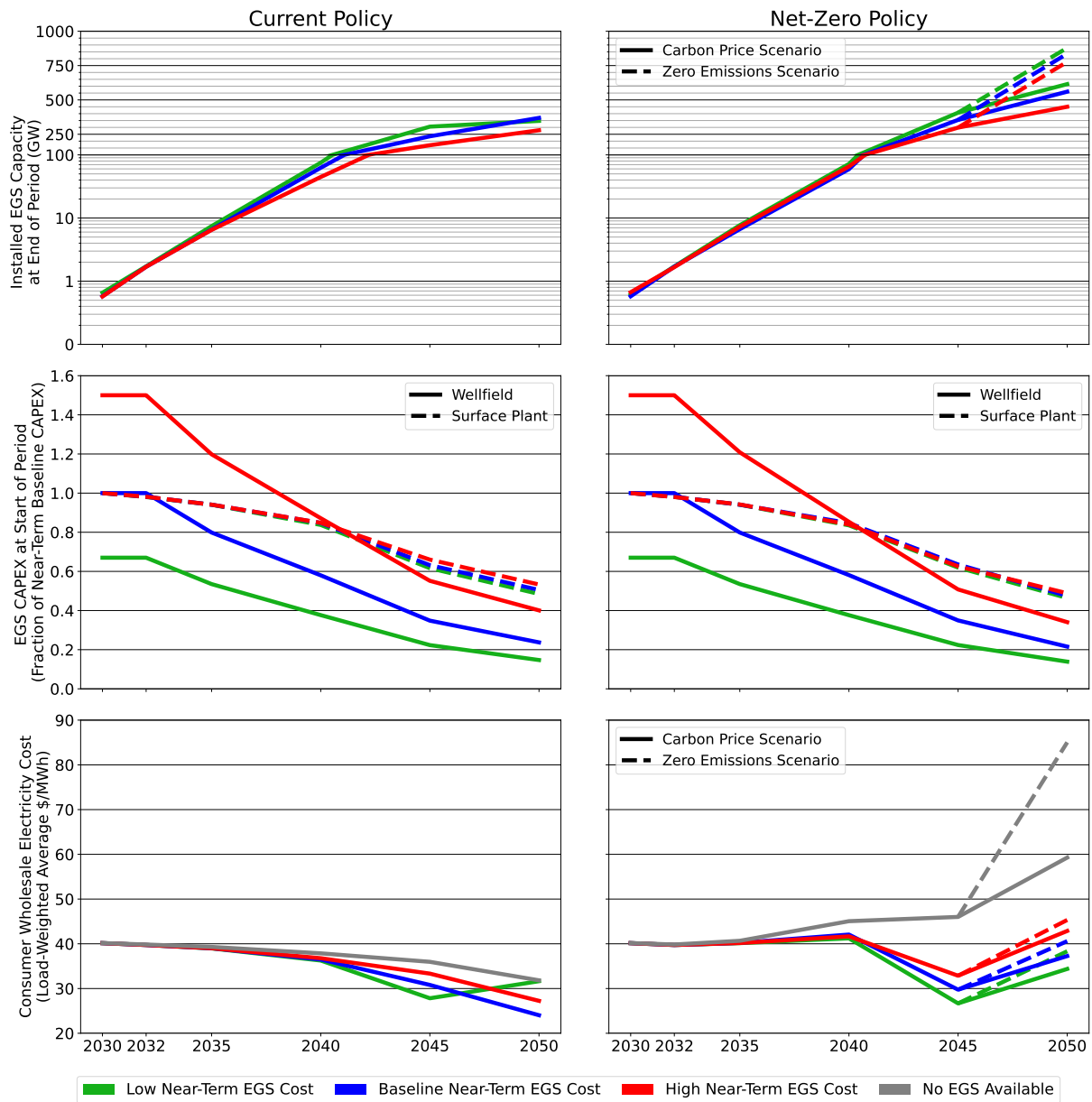


Figure S15: Same as Figure 2 in the main paper, for cases where an additional 20% adder is made available for firm carbon-free resources under the Section 48E Investment Tax Credit, and for carbon sequestration under the 45Q CCS tax credit. We note that the scenario with low EGS costs under current policies reaches the emissions threshold at which Inflation Reduction Act clean electricity tax credits phase out during the 2040-2045 planning period, leading to higher effective EGS costs in 2045-2050 and relatively lower deployment than in scenarios where the phase-out does not occur.

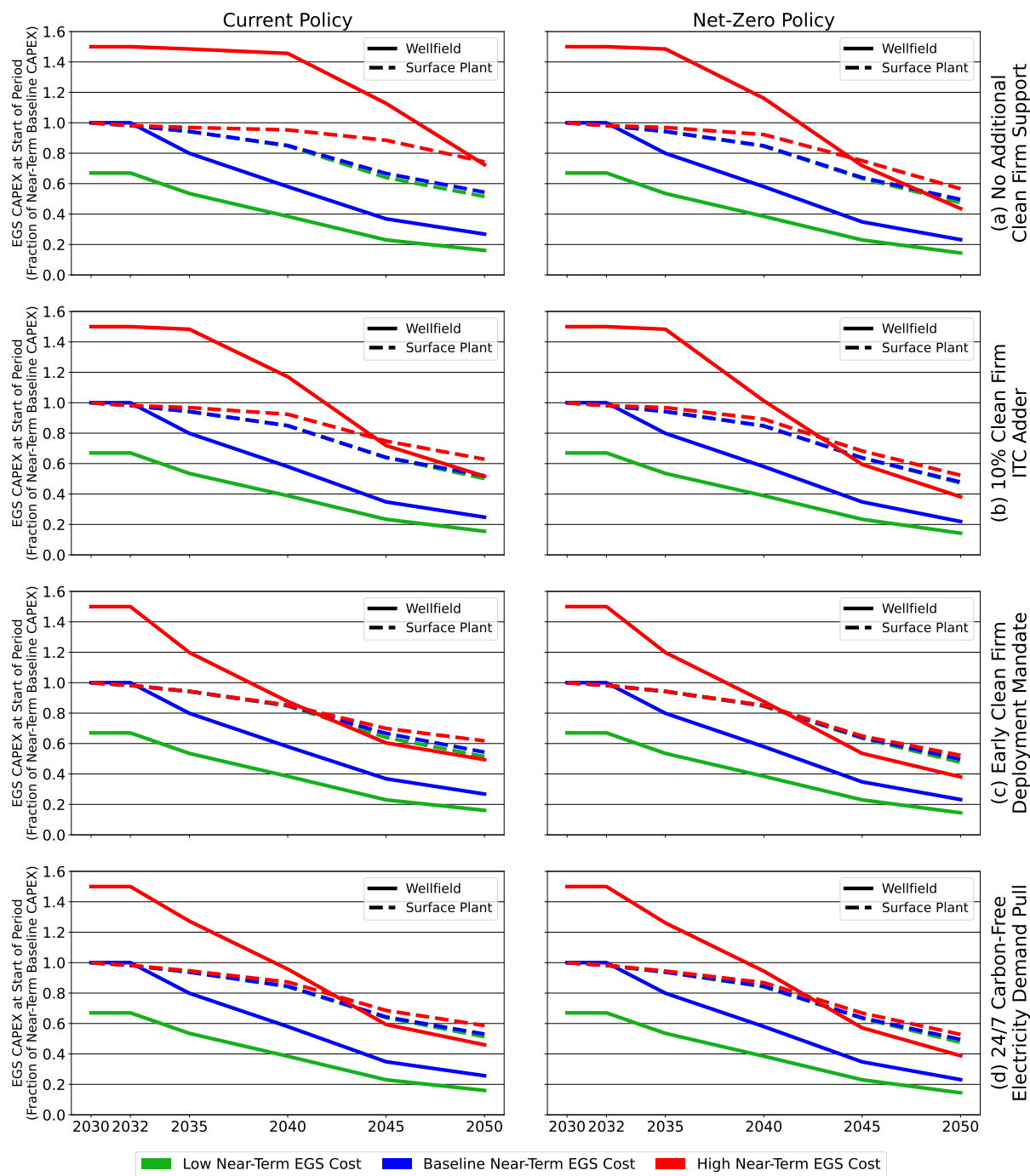


Figure S16: Trajectories of EGS capital costs for the same scenarios shown in Figure 6 in the main paper.

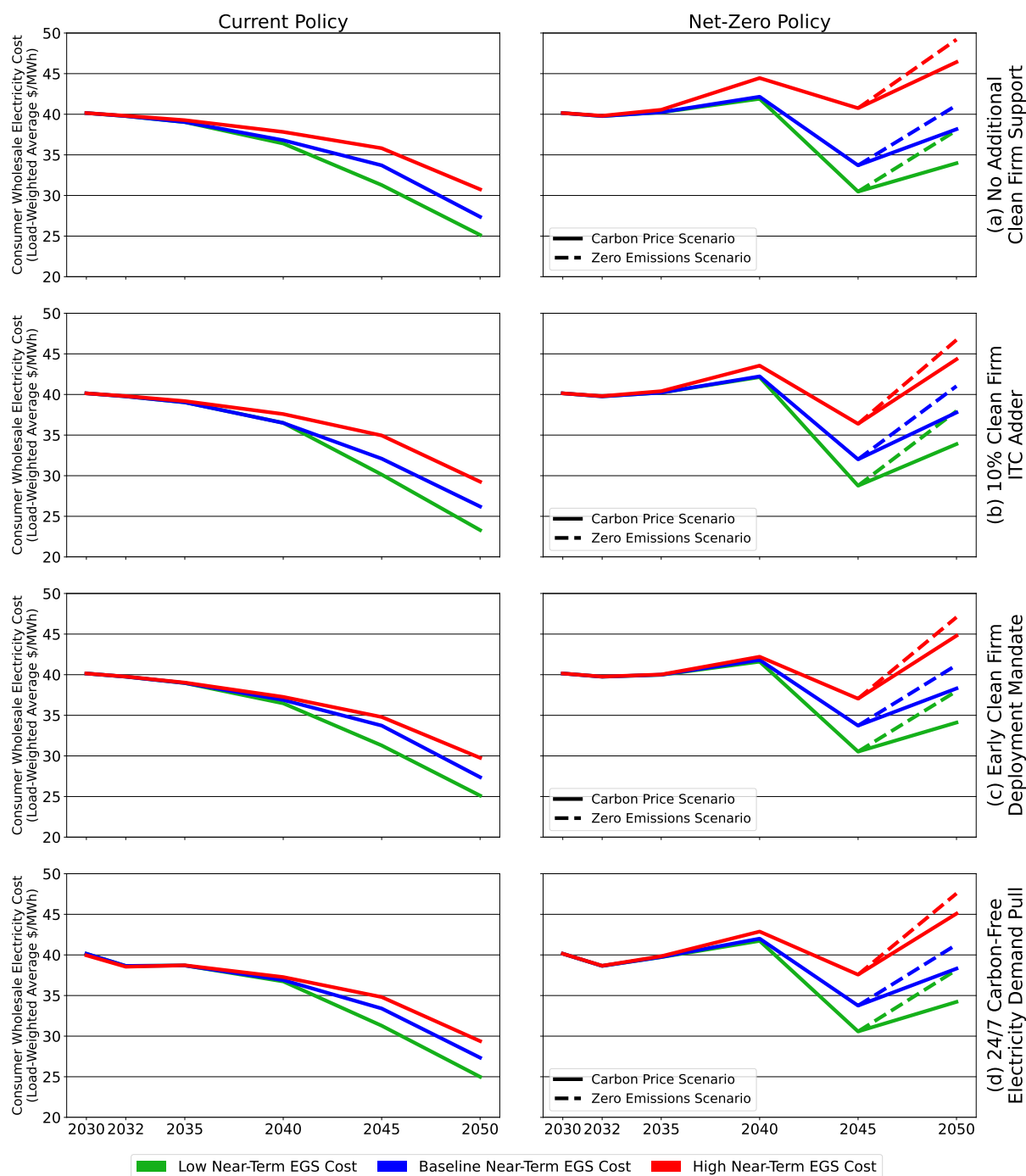


Figure S17: Trajectories of consumer electricity costs for the same scenarios shown in Figure 6 in the main paper.

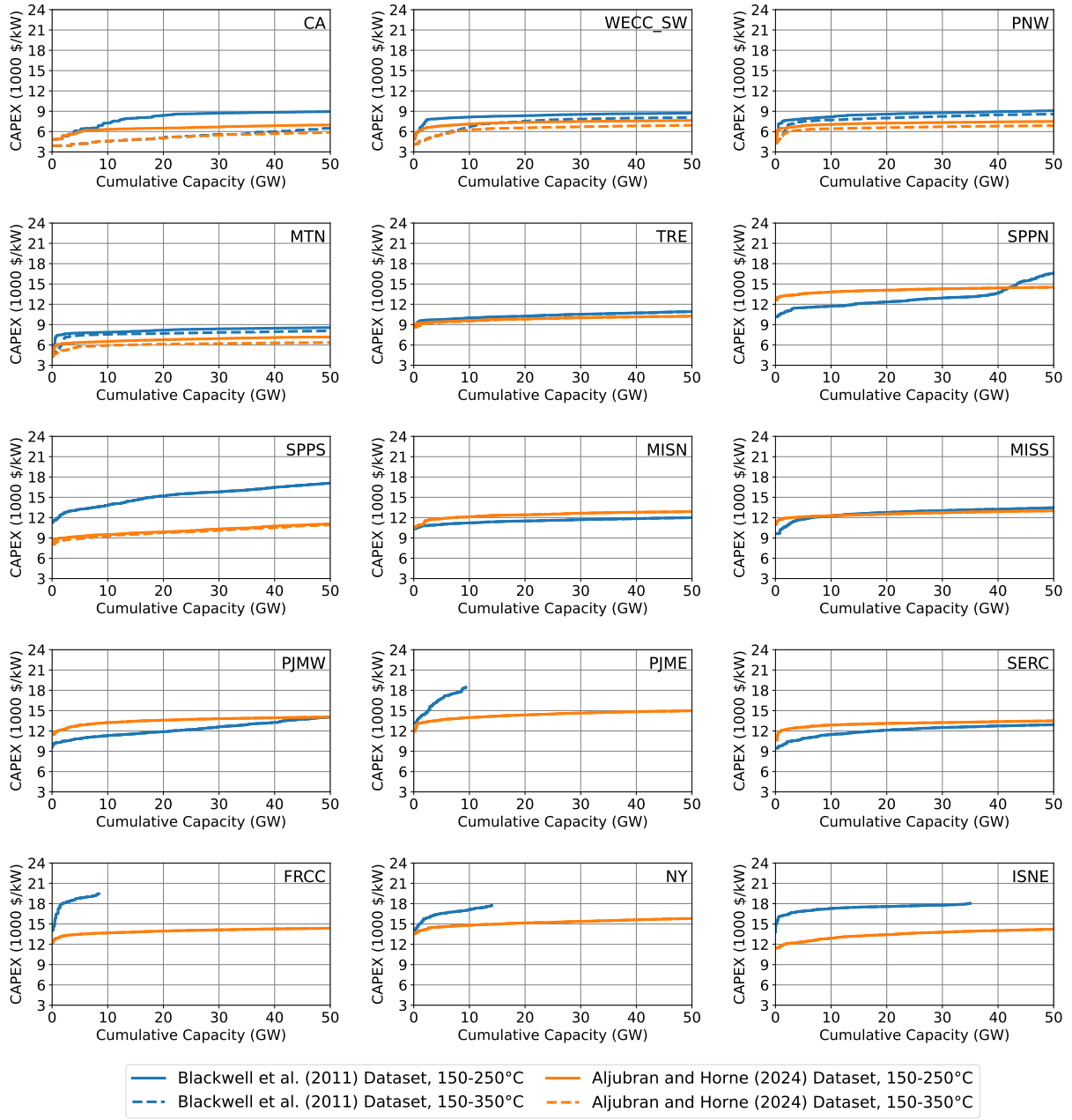


Figure S18: EGS supply curves for 15 US grid regions used in electricity sector capacity expansion modeling in this work (see Figure SS10), for resources in the 150-250°C and 150-350°C ranges, under baseline cost assumptions, using deep temperature-at-depth data from Blackwell et al.¹ and Aljubran and Horne².

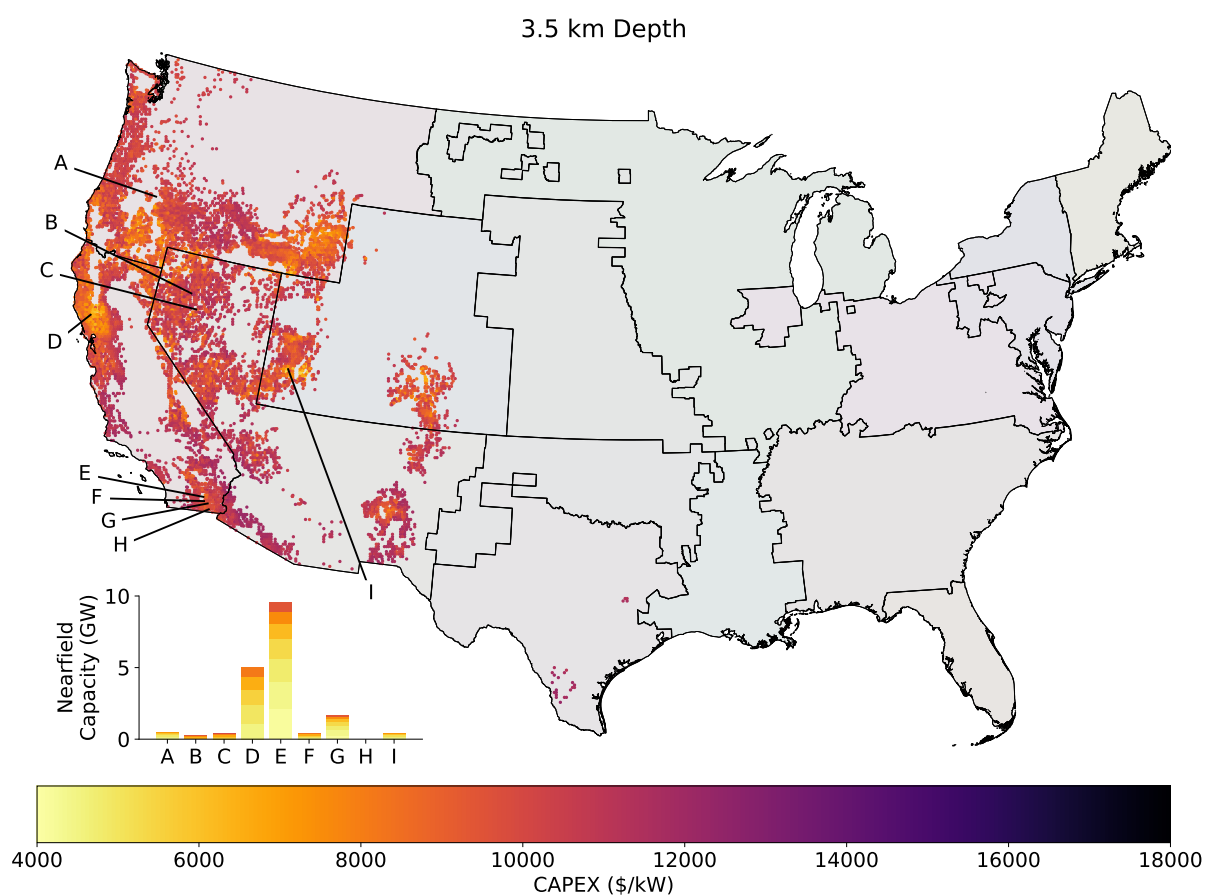


Figure S19: Map showing CAPEX for developable EGS capacity near nine large hydrothermal systems in the western US and at deep EGS candidate project areas nationwide (using temperature-at-depth data sourced from Aljubran and Horne²) at a depth of 3.5 km, for reservoir temperatures in the 150-350°C range, under baseline cost assumptions. Grid regions used in electricity sector capacity expansion modeling are also shown.

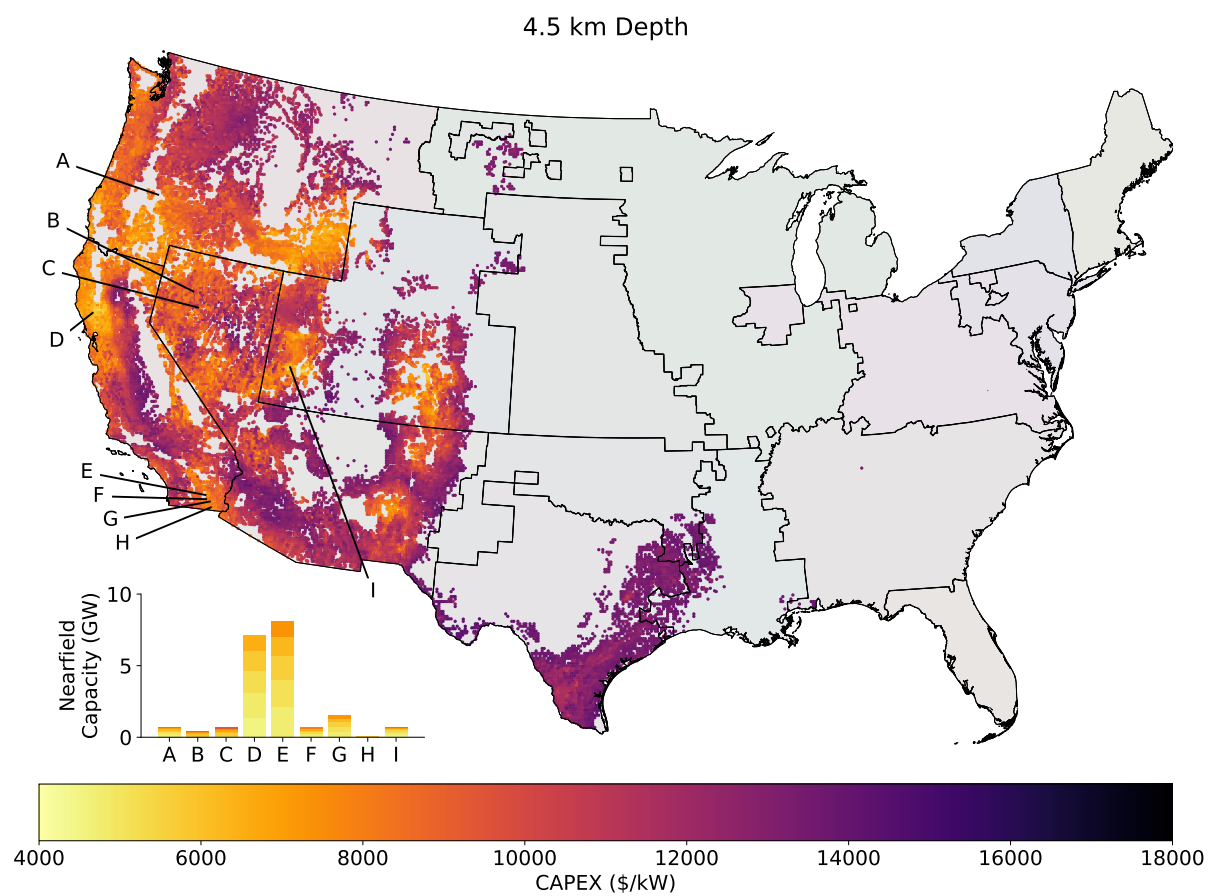


Figure S20: Same as Figure SS19, for resources at a depth of 4.5 km.

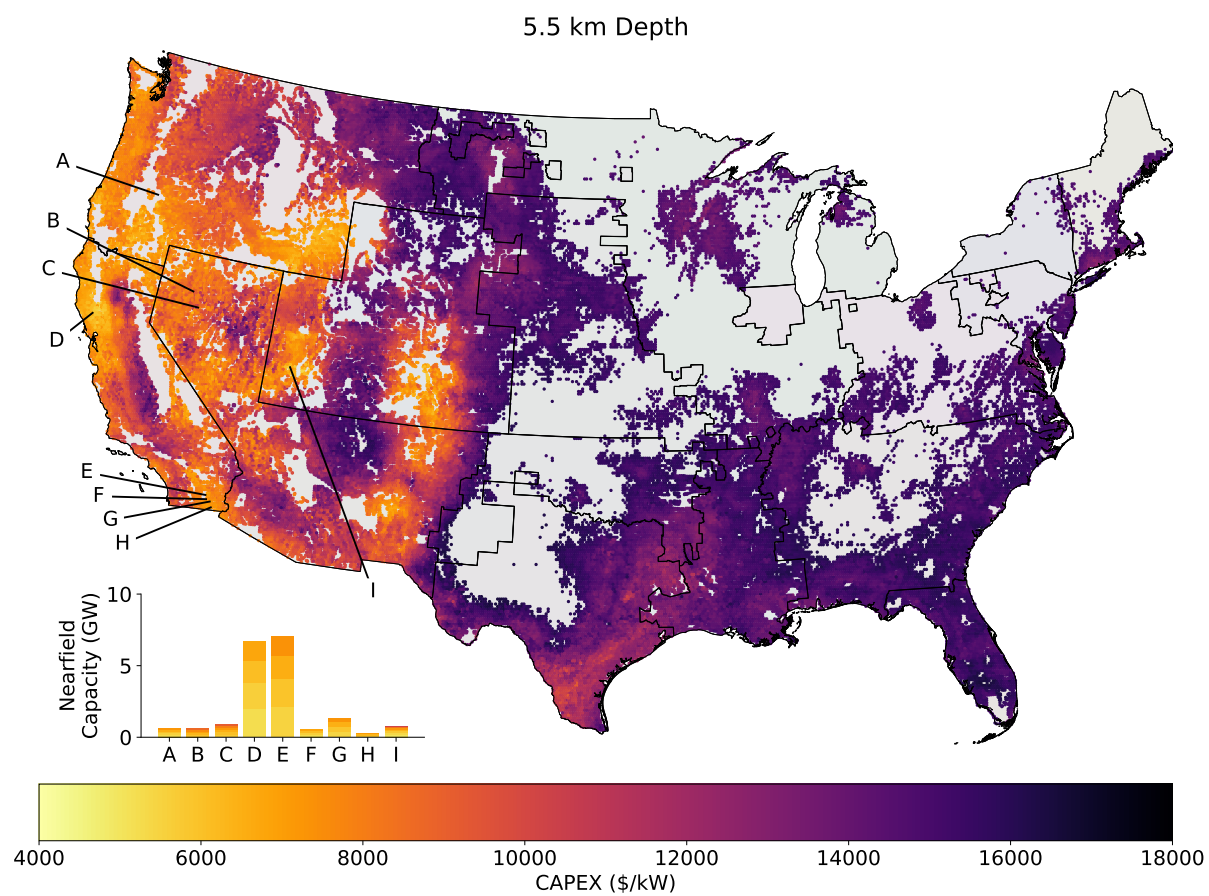


Figure S21: Same as Figure SS19, for resources at a depth of 5.5 km.

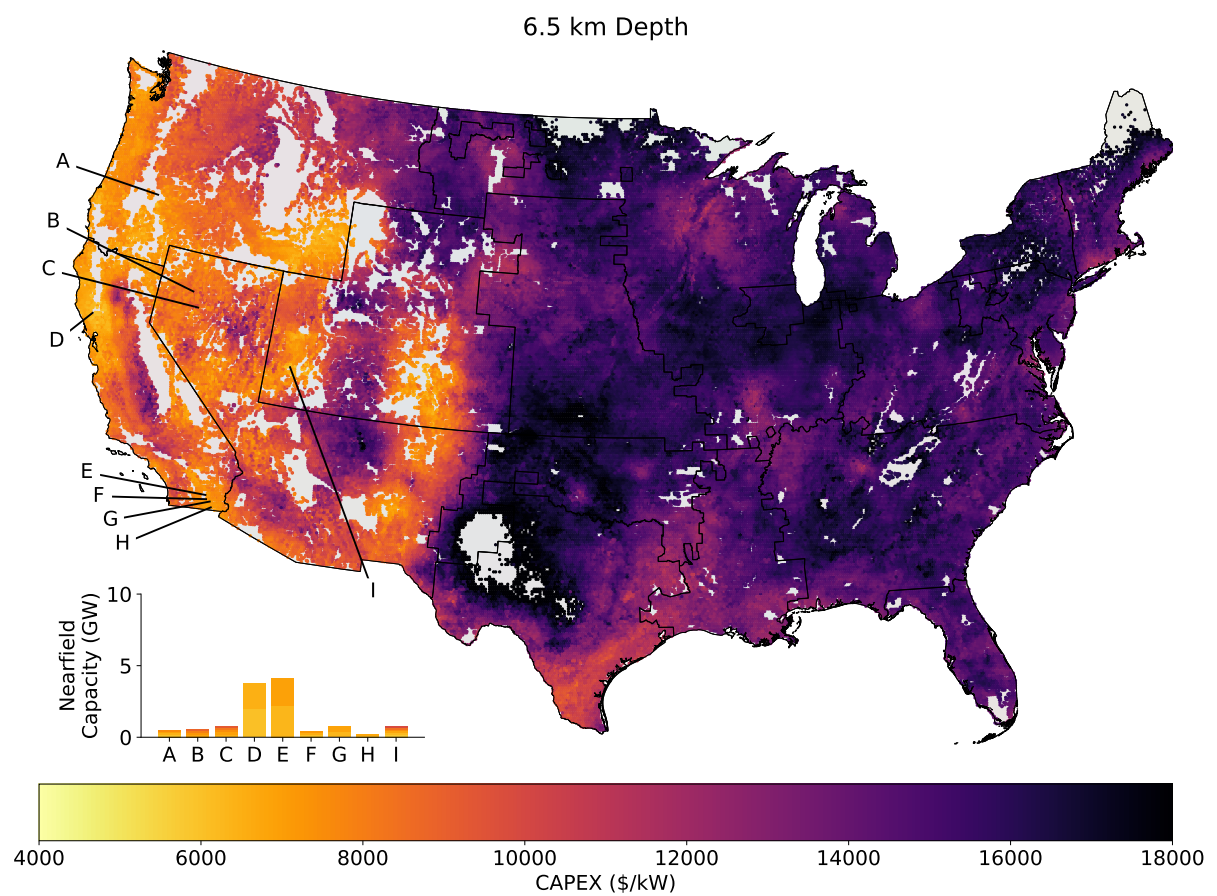


Figure S22: Same as Figure SS19, for resources at a depth of 6.5 km.

2 Supplementary Methods

2.1 EGS Cost and Performance Assumptions

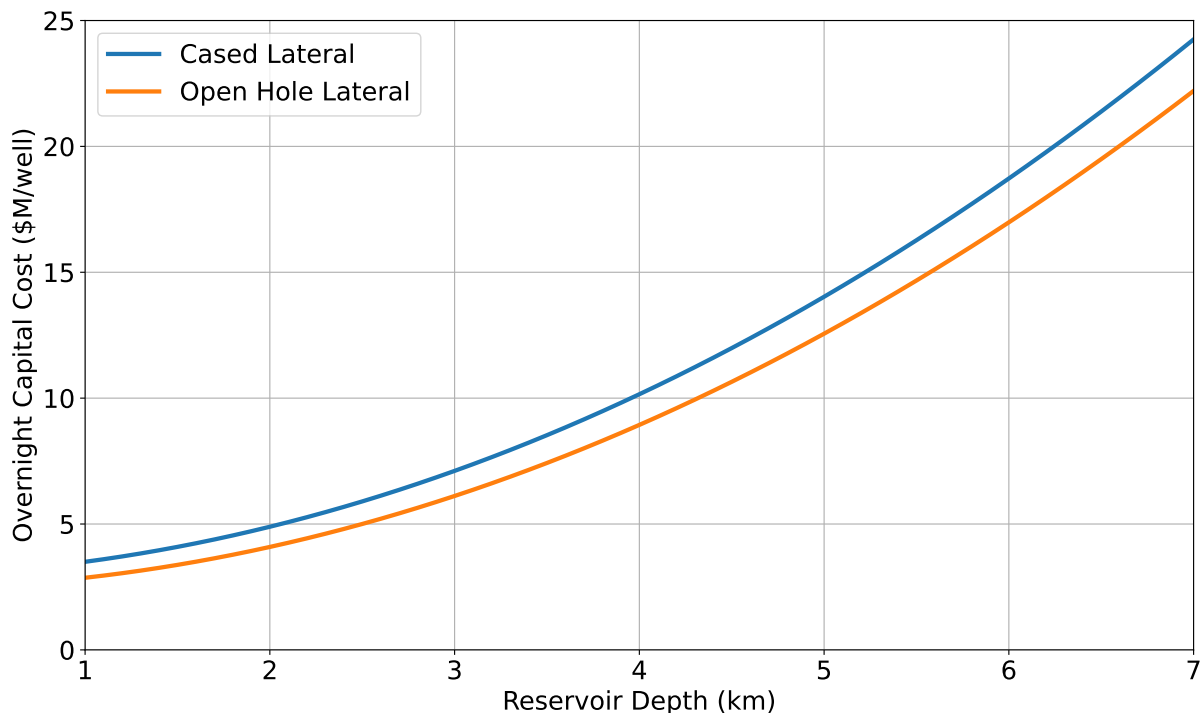


Figure S23: Drilling cost as a function of total vertical depth, for wells with 24.4 cm outer diameter and 2.29 km lateral length. Laterals are assumed to be cased by default, and open hole completion is only used if laterals are not stimulated (e.g. in Figure 9 of the main text).

We use results from numerical EGS reservoir simulations described in Ricks et al.³ to calculate a thermal decline profile for the reservoir over a 30-year operational lifetime and the impact of this decline on a plant's net present value. While the simulations from Ricks et al.³ predict an average thermal decline of 28°C (or a 44% decline in power output) after 30 years of operation for a reservoir with 2.29 km lateral length, 0.34 km lateral spacing, and a 160 l/s flow rate per injection well, these simulations assumed a perfectly uniform fracture network that is unlikely to be replicated in real-world EGS reservoirs. Because nonuniformities in fracture structure and flow rate can accelerate thermal decline compared to uniform systems, we assume here that the 28°C decline occurs after 25 years rather than 30, leading to a 35°C decline in temperature (or a 58% decline in power output) after 30 years. Using a real weighted average cost of capital for EGS projects of 5.48% adopted from NREL⁴, we calculate that this thermal decline leads to a 6.4% decline in the net present value of an EGS project. This reduction is applied to the modeled capacity factor of all EGS plants, as discussed in the following section. Because the reservoir design used in this paper has a lateral spacing 29% lower than the one simulated in Ricks et al.³, we reduce the steady-state flow rate in our assumed reservoir design by 23% to maintain the same thermal decline rate, using scaling relations for lateral spacing and flow rate from Doe and McLaren⁵.

In line with Ricks et al.³ and US DOE⁶, we assume that all EGS surface plants are air-cooled binary-cycle, offering zero emissions, greatly reduced water consumption, and increased operational flexibility compared to flash or dry steam plants. We update the surface plant cost model to calculate labor costs as a function of installed capacity, in line with Mines⁷, and adjust

labor and surface plant costs to the 2021 dollar year based on the relevant producer price indices. The full updated EGS cost model incorporating these and the above assumptions is available as a Python script at Ricks and Jenkins⁸, alongside all other relevant input data and results for the present study.

2.2 EGS Supply Curves

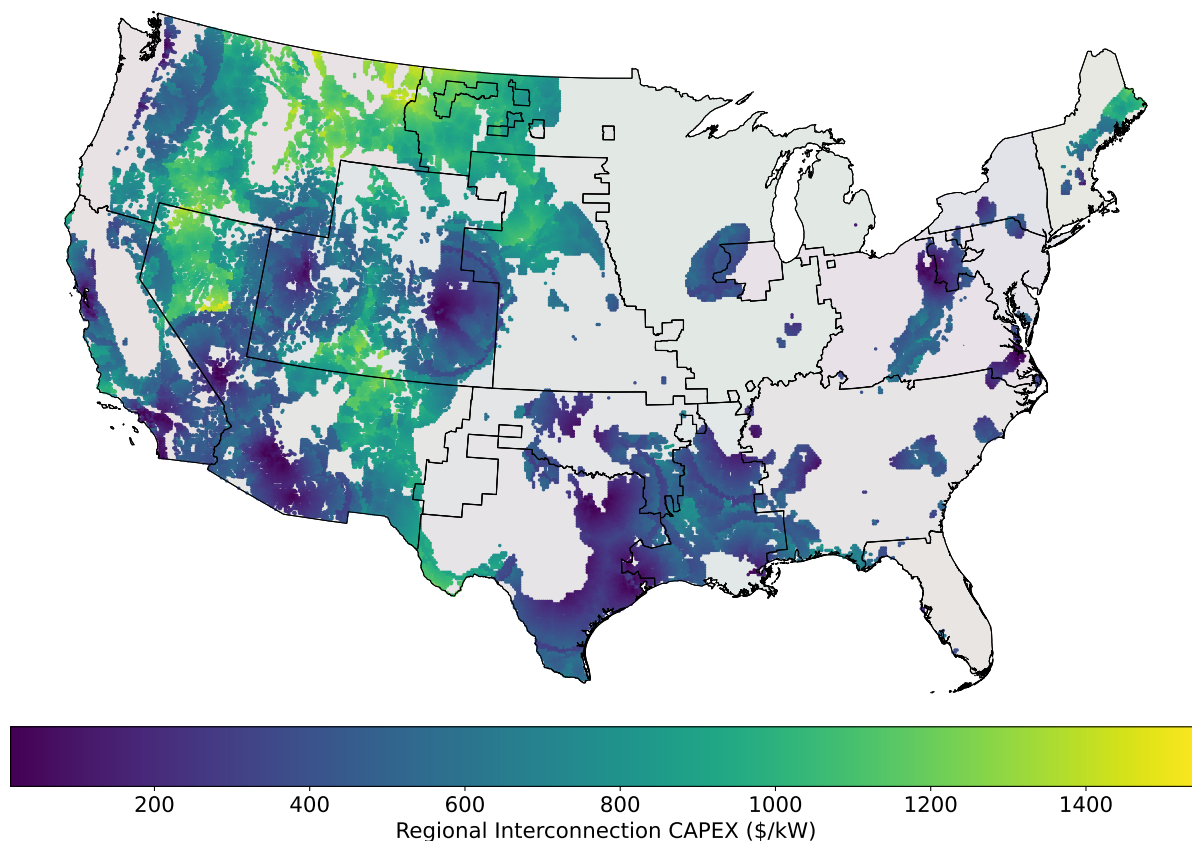


Figure S24: Map of regional grid interconnection costs for all EGS CPAs without land use barriers and with resource temperatures greater than 150°C at 6.5 km depth in the Blackwell et al.¹ dataset.

We use the EGS cost model discussed above to calculate EGS cost and developable capacity for over 80,000 candidate project areas (CPAs) at depths of 3.5 km, 4.5 km, 5.5 km, and 6.5 km based on deep temperature-at-depth values from Blackwell et al.¹ and alternatively from Aljubran and Horne². Because the Aljubran and Horne² maps are provided for depths of 1-7 km at 1 km intervals, we linearly interpolate between layers to extract predicted values at the same depths as the Blackwell et al.¹ maps. We assume conservatively that each depth band can host a single 'layer' of reservoirs, and we further de-rate developable capacities for all CPAs by 80% to account for potential land acquisition challenges and subsurface barriers such as fault lines.

As noted in Aljubran and Horne², neither of these deep temperature-at-depth datasets explicitly models the highly convective thermal regimes found at and near hydrothermal sites, and both may thus severely underestimate temperatures in these regions. Because there exists no prior comprehensive assessment of this 'near-field' EGS potential, we use reservoir volume and temperature data for these systems from Williams et al.⁹ in combination with a detailed temperature-at-depth survey for the Roosevelt Hot Springs geothermal area in Utah (the site of

FORGE and ongoing private EGS demonstrations)¹⁰ to estimate the developable near-field EGS capacity at all known hydrothermal sites in the contiguous US. We use the Roosevelt data to assess the cross-sectional subsurface area that exists within different 25°C temperature bands at a depth of 2.5 km around this site, and compare these measurements with the volume and temperature of the hydrothermal reservoir as provided in Williams et al.⁹. We fit a linear relationship between these quantities (see ‘FORGETemp.xlsx’ in Ricks and Jenkins⁸ for details) and apply this relationship to all other hydrothermal sites in the Williams et al.⁹ dataset. While the relationship between temperature-at-depth and reservoir properties from Roosevelt is likely not perfectly representative of other near-field sites, we do find that it largely agrees with coarser estimates presented in MIT¹¹ of the near-field resource available near the large Geysers hydrothermal reservoir in northern California. While the Roosevelt relationship estimates an area of $\sim 900 \text{ km}^2$ at temperatures greater than 150°C near the Geysers at a depth of 2.5 km, the site-specific maps presented in MIT¹¹ suggest an area of just over 1000 km² at the same temperature and depth. In addition to near-field temperature-at-depth data for the 2.5 km depth band, we also use an assumed 50 C/km geothermal gradient (slightly more conservative than the 70 C/km observed at Roosevelt) to calculate similar values for depths of 3.5 km, 4.5 km, 5.5 km, and 6.5 km. We cut off near-field data at all depths for bands where the temperature is below either 150°C or the temperature of the nearest site at the same depth in the deep temperature-at-depth dataset. We apply the same costing methodology to near-field sites that is used for deep CPAs, but derate near-field resources by 60% rather than 80% to account for more established land rights and electricity system interconnections at these sites.

Finally, we calculate hourly capacity factor time series for each geothermal CPA for the 2012 weather year based on hourly surface ambient temperature data, following the same procedure outlined in Ricks et al.³. This calculation assumes that all surface power plants are air-cooled to minimize water consumption. We modify these time series by subtracting 6.4% from the effective output in each hour, reflecting the net present value impact of thermal decline in the reservoir over the lifetime of a project as described above.

2.3 EGS Model Structure and Inputs

As discussed above, we modify the public release of the GenX model in this work to incorporate the flexible EGS module described in Ricks et al.³. This module allows for optimization of the sizing of individual EGS plant components and of well flow rates in each modeled timestep. Optimized components include wellfield capacity, surface binary-cycle power plant capacity, grid interconnection capacity, and injection pumping power capacity. To limit model complexity we do not model or optimize the sizing of surface storage for excess produced geofluid, as results from Ricks et al.³ indicate that this component typically accounts for less than 1% of the total cost of an EGS plant. In addition to component sizing, the model optimizes injection and production flow rates for each EGS resource in each timestep, tracking the evolution of reservoir pressure across timesteps via a formulation that accurately captures the pressure behaviors observed in numerical reservoir simulations^{3,12}. Pressure metrics at injection and production well bottomholes are used to calculate parasitic injection pumping power requirements and maximum achievable production flow rates at each timestep, respectively. The full mathematical formulation of the model is provided in Ricks et al.³, and a schematic illustrating the optimized components is shown in Figure SS25.

In this paper we use the same default model parameters as Ricks et al.³, with the following exceptions. First, we enforce a minimum production flow rate of 10% of the steady-state production rate for all EGS facilities, reflecting the need to avoid thermal cycling from full production shutdowns that could harm wellbore integrity^{13,14}. Second, we adjust parameters for

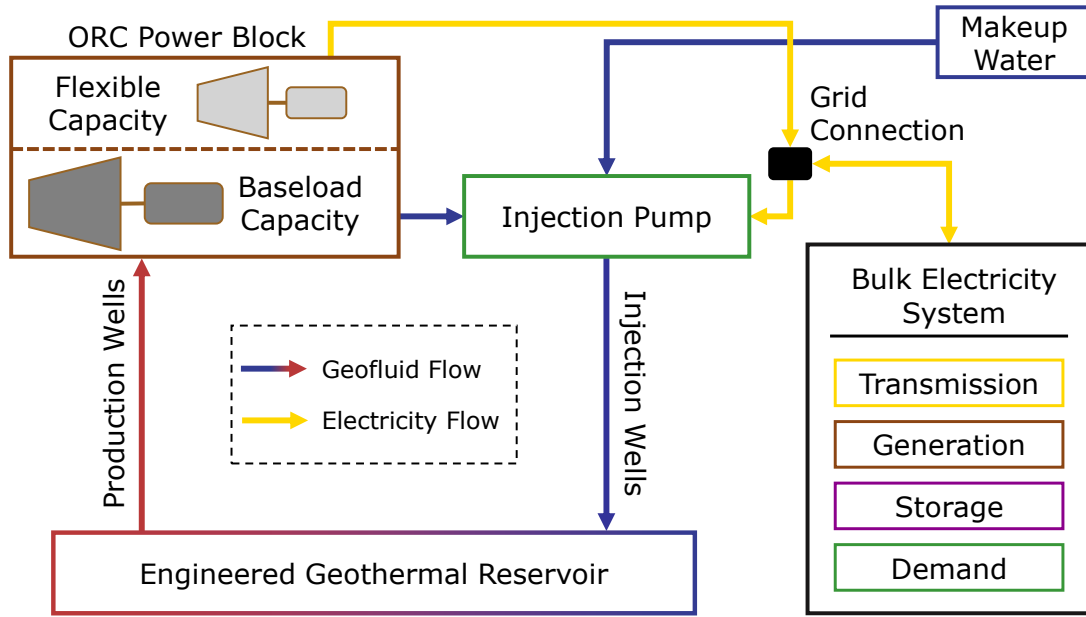


Figure S25: Schematic diagram of the flexible EGS optimization model used in this work. EGS power plant investments and operations are optimized in tandem with other bulk electricity system components in GenX.

the pressure differential across the reservoir during steady-state operation to reflect the fracture conductivity values calculated from field tests as described above. We use a power law fit of cross-reservoir pressure differential values from the same set of EGS reservoir simulations described in Ricks et al.³ to calculate the expected pressure differential for a $1.2 \times 10^{-13} \text{ m}^3$ fracture conductivity value under the same operating conditions, then scale this down to reflect the smaller lateral spacing and flow rate in our baseline reservoir design using Darcy's law (see calculations in 'Scenario_Params.xlsx' in Ricks and Jenkins⁸).

Finally, we use field data from the EGS demonstration project circulation test discussed in Norbeck and Latimer¹⁵ to calibrate the expected pressure response of real EGS reservoirs under flexible operation. As part of this circulation test production and injection flow rates were intermittently modulated over a multi-day period to assess the performance of the system under flexible operating conditions. We select one of these cycles, in which the production flow rate was dropped from approximately 45 l/s to 0 l/s and held at that level for 10 hours while the injection rate remained constant, and use the recorded reservoir pressure response over this period to calibrate the sensitivity of our modeled reservoir bottomhole pressure to changes in flow rates, as described in Ricks et al.¹² and Ricks et al.³. While the 10 hour duration is not long enough to provide sufficient input data for the model (at least 50 hours is required), we observe that it is nearly identical in shape to the simulated pressure response functions used in Ricks et al.³ over that 10-hour period. We therefore use the observed pressure response to scale the simulated response function (choosing the function from the 'Low Subsurface Favorability' simulation described in Ricks et al.³ due to its similar shape), taking into account the different geometries of the field test reservoir and the simulated reservoir. We assume that to first order, the magnitude of the pressure response to a given change in flow rate is directly proportional to the total fracture surface area in the reservoir. Further assuming a similar number of active fracture pathways per unit of lateral length between the actual and simulated reservoirs (based on the number of individual perforations used in stimulation¹⁵), we compare the length and cross-sectional dimensions of the reservoirs to obtain a scaling factor (see 'Field.Coeffs.xlsx' in Ricks

and Jenkins⁸). In this calculation we assume that fractures at the field site occupy the full 0.11 km by 0.24 km cross-sectional area between the injection and production laterals, and half of the 0.24 km by 0.24 km area implied by reported fracture half-length and half-height measurements on the outside of each lateral. The re-scaled field pressure response function is shown alongside the simulated response function for the ‘Low Subsurface Favorability’ case from Ricks et al.³ in Figure SS26, and indicates a slightly more muted pressure response to changes in flow than the simulation. We use this scaled response function for all flexible EGS plants modeled in this work, while recognizing the need for further field testing to fully characterize and bound the real-world behavior of these systems.

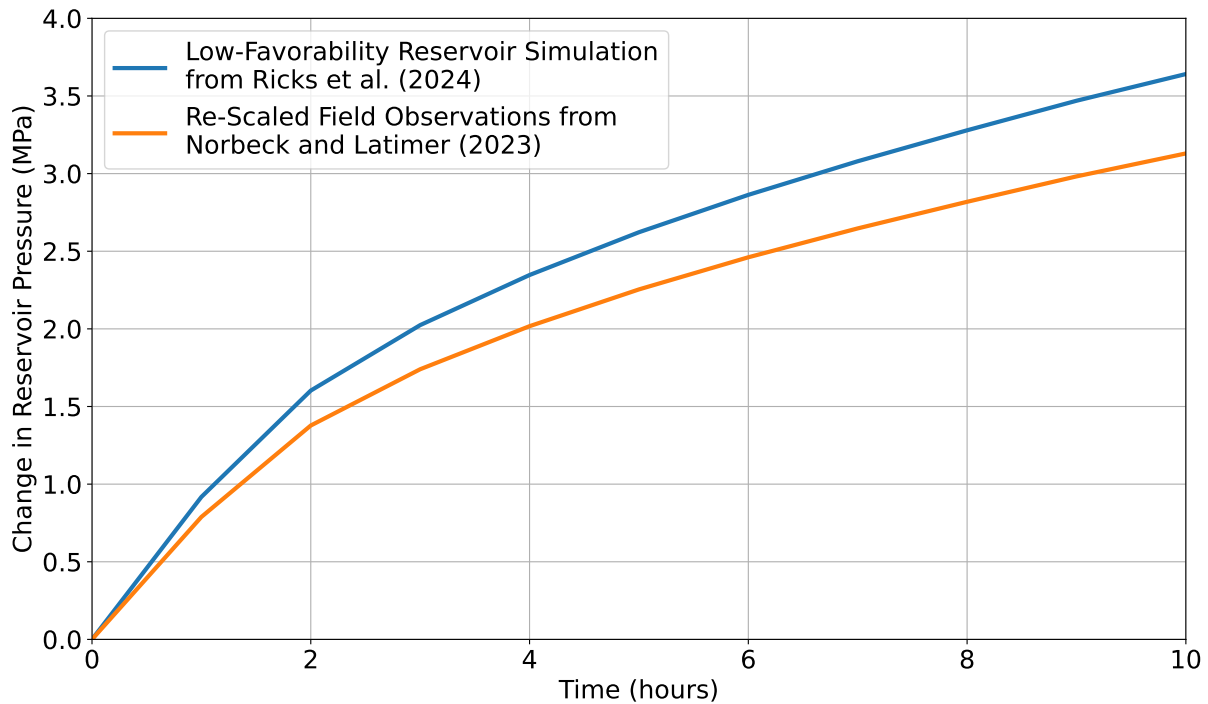


Figure S26: Comparison between the 10-hour simulated reservoir pressure response resulting from an instantaneous reduction in production flow rate of 160 l/s from Ricks et al.³, and field data from Norbeck and Latimer¹⁵ that have been re-scaled to account for differences in flow rate and reservoir geometry.

To represent the very large number of EGS CPAs in the GenX model while maintaining computational feasibility, we group individual CPAs into larger clusters with similar characteristics. We first divide the full set of EGS CPAs into groups assigned to each GenX model zone, with zone assignment based on the regional grid to which the CPA can be interconnected at least cost (rather than the CPA’s physical location). Figure SS27 shows the full set of developable EGS CPAs for the Blackwell et al.¹ temperature-at-depth dataset broken down by assigned zones. Next, within each zone we divide CPAs into near-field and deep groupings, and subsequently by depth. Within each of these subgroups, we then apply a k-means clustering algorithm to group CPAs into a specified number of clusters with a specified maximum total capacity, such that variance in total annuitized per-kW cost within each cluster is minimized. For each cluster, all parameters are equal to the capacity-weighted average of the same parameters from its component CPAs. Each cluster is then assigned flexible EGS model parameters based on its temperature and depth following the procedure outlined in Ricks et al.³ with the modifications described above. Finally, because this procedure creates a very large number of total clusters, we filter the full set by total annuitized cost before each GenX planning period to select only the least-cost options up to a specified maximum total capacity in each model zone, as well as those

that had seen buildout of 50 MW or more in previous periods. The total number of selected EGS clusters varies, but is typically between 150 and 350 in each planning period.

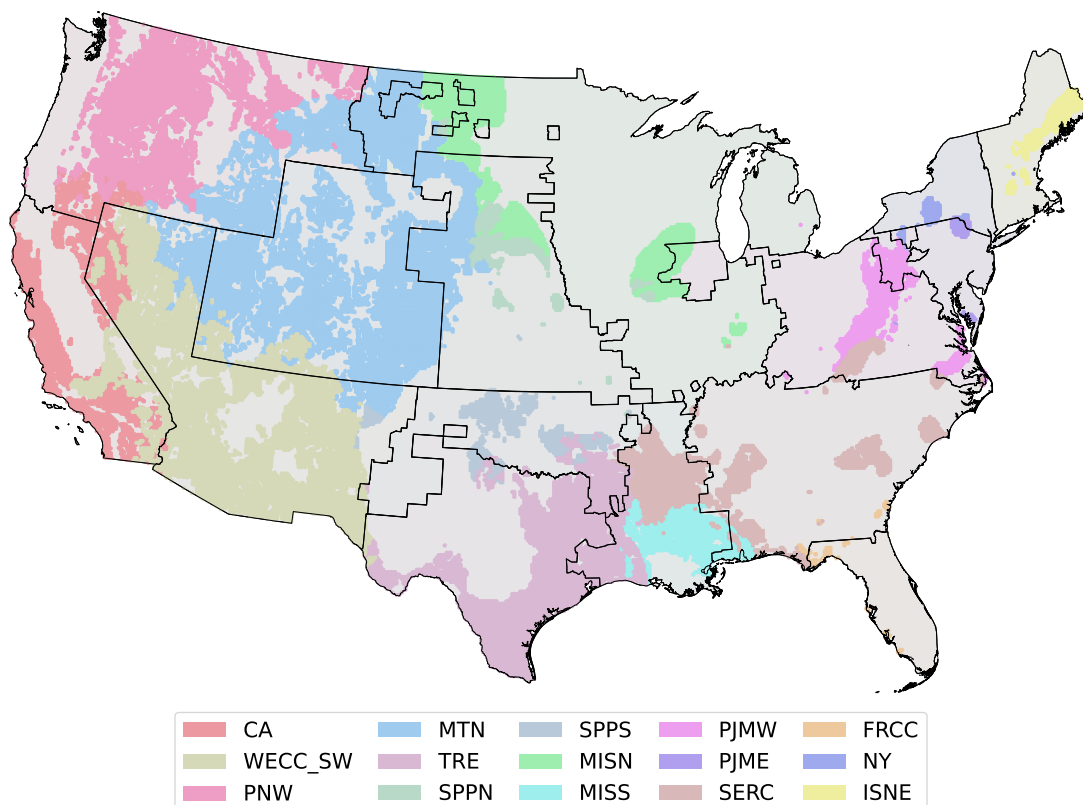


Figure S27: Map showing assignment of developable EGS CPAs in the Blackwell et al.¹ dataset to the GenX model zones shown in Figure SS10, based on least-cost interconnection pathways.

2.4 Capacity Expansion Model Modifications

As noted in Section 4.3 of the main paper, we model the evolution of the electricity sector in this work using a modified version of the v0.3 release of the open-source GenX electricity system capacity expansion model. Documentation for the public release of GenX is available at <https://genxproject.github.io/GenX.jl/stable/>, including the full mathematical formulation of the model. In this section we discuss modifications made to the public release of GenX (separate from the addition of the flexible EGS module discussed in the prior section and³), primarily constraints dealing with hourly-matched electricity supply and exogenous demand for clean hydrogen. First, we introduce the following notation:

Table S1: Sets, variables, and parameters relevant to modifications of GenX in this work.

Notation	Description
$t \in T$	Where t denotes an hour in the modeled weather year.
$z \in Z$	Where Z is the set of all model zones.
$y \in G$	Where G is the set of all generation and storage resources.
O	The set of all storage resources.
Q	(New) the set of all clean resources qualified to serve time-matched carbon-free electricity demand.
E	(New) the set of all electrolyzer and hydrogen storage resources.
$\Theta_{y,z,t}$	Generation by resource y in zone z at timestep t .
$\Pi_{y,z,t}$	Charging by storage resource y in zone z at timestep t .
$\Gamma_{y,z,t}$	Energy stored by storage resource y in zone z at timestep t .
$\Upsilon_{y,z,t}$	(New) exogenous use of energy stored by storage resource y in zone z at timestep t .
η_y^{loss}	Self-discharge rate of storage resource y .
η_y^{charge}	Charging loss rate of storage resource y .
$\eta_y^{discharge}$	Discharging loss rate of storage resource y .

Next, we modify the standard storage charge balance constraint in GenX to include a variable Υ denoting stored energy that is extracted for some other use rather than converted back into electricity:

$$\Gamma_{y,z,t} = \Gamma_{y,z,t-1} - (1/\eta_y^{discharge} * \Theta_{y,z,t}) - \Upsilon_{y,z,t} - (\eta_y^{loss} * \Gamma_{y,z,t}) + (\eta_y^{charge} * \Pi_{y,z,t}) \quad (1)$$

In this work, hydrogen electrolysis is represented as a storage device from which some amount of the stored energy can be removed for direct use. We also introduce a constraint requiring the use variable Υ to be equal to some exogenously fixed value U in each zone and timestep, representing an exogenously fixed hydrogen demand:

$$\Upsilon_{y,z,t} = U_{y,z,t} \quad (2)$$

Finally, we introduce a universal *hourly matching* constraint, which requires that the net of generation and charge from all resources in the tagged set Q be greater than or equal to some exogenously fixed value H in each zone and timestep:

$$H_{z,t} \leq \sum_{y \in Q} \Theta_{y,z,t} - \sum_{y \in (O \cap Q)} \Pi_{y,z,t} \quad (3)$$

In this equation H is typically set to 0, effectively only requiring that all power used to charge hydrogen storage (for direct use or conversion back to electricity) be sourced from clean resources. In one sensitivity case we use a nonzero value for H to represent additional demand for time-matched clean generation.

2.5 Non-EGS Input Data

The majority of non-EGS cost, system structure, and demand data used as inputs for the GenX model in this work are compiled using the PowerGenome tool¹⁶. PowerGenome sources projected cost, lifetime, and financial parameters for onshore and offshore wind power, solar photovoltaic power, lithium ion batteries, combined cycle gas power plants, and open-cycle gas combustion turbines from the 2024 edition of the US National Renewable Energy Laboratory's Annual Technology Baseline (ATB)⁴, using the 'Moderate' cost case and 'Market Factors' financial case for all technologies. For each planning period, technology cost inputs in GenX reflect the average of ATB costs for all years in that period. Capital costs for each new-build technology are modified by regional cost multipliers from the US Energy Information Administration's Annual Energy Outlook (AEO)², and costs for wind and solar CPAs are modified to reflect regional grid interconnection costs using the same transmission routing workflow described above in the case of EGS CPAs (we also apply AEO regional cost multipliers to emerging nuclear and Allam cycle gas technologies). Wind, solar, and lithium ion battery costs for the 'Low VRE and Battery Cost' and 'High VRE and Battery Cost' are taken from the ATB's 'Advanced' and 'Conservative' cost cases, respectively. Regional fuel costs for each planning year are taken from the AEO's 2022 'Reference' case, and fuel costs for the 'High Natural Gas Price' and 'Low Natural Gas Price' sensitivity scenarios shown in Figure 7 in the main paper are taken from the 'Low Resource' and 'High Resource' cases, respectively¹⁷ (see Figure SS28). New-build and existing wind and solar sites, as well as existing thermal power plants, are grouped into clusters of similar projects using the same k-means clustering approach applied to EGS above, though without the need to filter by resource temperature and depth. Costs for hydrogen electrolyzers and geologic storage are not provided in the ATB, and are instead adopted from other sources. Following ?, we assume that electrolyzer costs start at \$1800/kW at present, decline linearly to \$900/kW by 2030 and \$600/kW by 2035, and by 0.5%/yr thereafter. Input electrolyzer costs by planning

Planning Period	Electrolyzer CAPEX (\$/kWe)
2024-2030	1350
2030-2032	840
2032-2035	690
2035-2040	593
2040-2045	578
2045-2050	564

Table S2: Input capital cost for hydrogen electrolysis by model planning period.

period are shown in Table S2. We adopt a cost of \$2/kWh for geologic hydrogen storage from Viswanathan et al.¹⁸, and apply this cost in all model regions across all planning periods. We assume a universal electrolyzer efficiency of 65%, inclusive of electricity used in compression for storage. In the ‘Low Electrolyzer Cost and High Hydrogen Demand’ and ‘High Electrolyzer Cost and Low Hydrogen Demand’ sensitivity scenarios shown in Figure 7 in the main paper, we modify electrolyzer fixed costs by -25% and +33%, respectively. Hydrogen combustion turbine cost and efficiency assumptions are identical to those used for natural gas combustion turbines, leading to an overall round-trip electricity storage efficiency of 23%. For hydrothermal resources, we calculate costs for sites with remaining developable capacities greater than 50 MW listed in Williams et al.⁹ using the EGS cost model described above, with the following modifications: costs for well laterals and stimulation are both removed, surface plant unit size is decreased from 50 MW to 25 MW, and all reservoirs are assumed to be at 2.5 km depth. All input data described above and the scripts used to compile it are available at Ricks and Jenkins⁸. Cost assumptions for Allam cycle gas plants and nuclear SMRs are discussed in the main text.

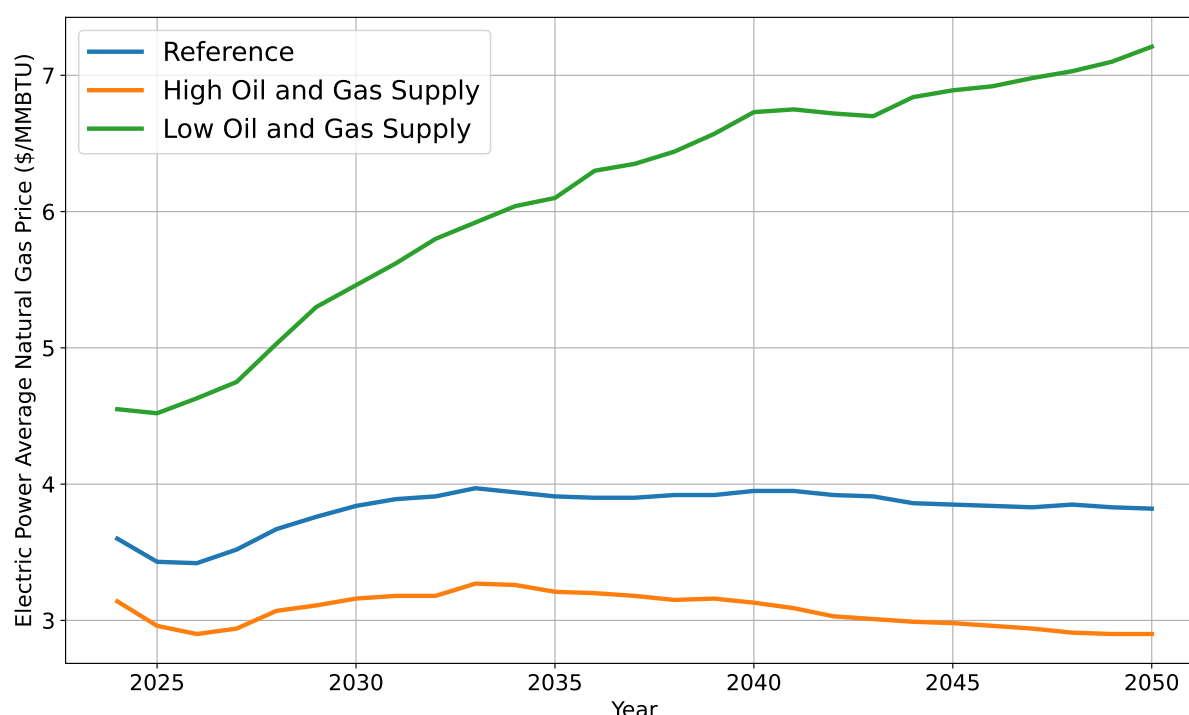


Figure S28: Natural gas price inputs (including sensitivities) from the EIA Annual Energy Outlook 2022.

We adopt up-to-date state-level renewable portfolio standard (RPS) and clean energy standard (CES) policy requirement inputs for each planning year from Gagnon et al.¹⁹. For states

or regions with carbon cap-and-trade policies covering the electricity sector (model zones CA, ISNE, NY, PJME, and PNW in Figure SS10), given non-modeled interactions with other economic sectors and deep uncertainties in future allowance prices, we assume a fixed allowance price of \$20/tCO₂ in all planning periods. At the federal level we model two broad sets of scenarios, ‘Current Policy’ and ‘Net-Zero Policy’. Both scenarios use electricity and exogenous electrolytic hydrogen demand inputs adopted from the mid-range, current policy case from Jenkins et al.²⁰ for planning periods through 2035. These inputs continue to be used in the Current Policy scenario from 2036 onward, while the Net-Zero scenarios switch to inputs adopted from the net-zero pathway benchmark case from Jenkins et al.²⁰. These demand trajectories are shown in Figure SS29. In the ‘Low Electrolyzer Cost and High Hydrogen Demand’ and ‘High Electrolyzer Cost and Low Hydrogen Demand’ sensitivity scenarios shown in Figure 7 in the main paper, we modify exogenous hydrogen demand by +33% and -25%, respectively. For both current and net-zero policy scenarios we model electricity production, CCS, and clean hydrogen production subsidies put in place under the Inflation Reduction Act (IRA)²¹. We model section 45U tax credits for existing nuclear power plants as a mandate to keep these plants online through 2032. The section 45Q CCS credit and section 45V clean hydrogen production tax credit (PTC) are applied to all carbon sequestration by Allam cycle gas plants and qualifying clean hydrogen production from electrolyzers through 2035, accounting for safe harbor allowances after the official expiry of these credits in 2032. Subsidized clean hydrogen production is required to meet temporal and location matching requirements designed to minimize induced emissions, with locational matching occurring at the level of individual model zones. The Section 45Y PTC and Section 48E investment tax credit (ITC) for carbon-free electricity production and storage are applied through 2035 or whichever model stage sees US electricity sector greenhouse gas emissions fall below 25% of 2022 emissions at an absolute level, or roughly 0.38 GtCO₂e/yr. Emissions results are checked at the end of each model stage to determine whether the 45Y and 48E subsidies remain in effect in the following stage. Onshore wind and solar resources are assumed to select the Section 48E ITC, and lithium-ion battery, geologic hydrogen storage, offshore wind, hydrothermal, EGS and nuclear SMR resources are assumed to select the 45Y PTC. We assume that all projects meet prevailing wage requirements necessary to unlock the full base credit value. We further assume that all battery, hydrogen storage, offshore wind, hydrothermal, EGS, and nuclear SMR resources benefit from a 10% credit adder for domestic manufacturing, and that nuclear SMR plants can always be preferentially sited to qualify for an additional 10% credit adder for projects located in ‘energy communities.’ For hydrothermal and EGS resources we map individual CPAs to energy communities as defined in ? and apply the appropriate ITC adder to CPAs that fall within the geographic boundaries of these communities. For For wind and solar resources we assume that domestic manufacturing credit benefits largely cancel out the additional cost of domestic over foreign manufacturing, and we therefore do not apply the PTC domestic manufacturing adder for these resources. We use the same mapping approach as for geothermal CPAs to determine qualification of each wind and solar CPA for the PTC energy communities adder. For all resources receiving 45Y credits, we assume that 7.5% of the credit value is lost in the process of monetization. For all resources receiving a PTC (either 45Q, 45V, or 45Y PTCs) where the PTC credit period is shorter than the resource’s financial lifetime, we reduce the modeled value of the credits to reflect an equivalent net present value if applied over the full lifetime of the resource. For hydrogen electrolyzer projects, because the 45V credit represents the vast majority of project revenue, we assume that project financial lifetime is reduced to the PTC length of 10 years rather than the typical 30 while 45V is in effect.

For clean firm policy sensitivity cases shown in Figure 6 in the main paper, we modify model inputs as follows. In the ‘10% Clean Firm ITC Adder’ case, we include a further 10% adder to the 48E ITC for EGS, hydrothermal, and nuclear SMR resources. While we assume that Allam cycle gas plants do not receive 48E due to upstream methane emissions, we increase the 45Q

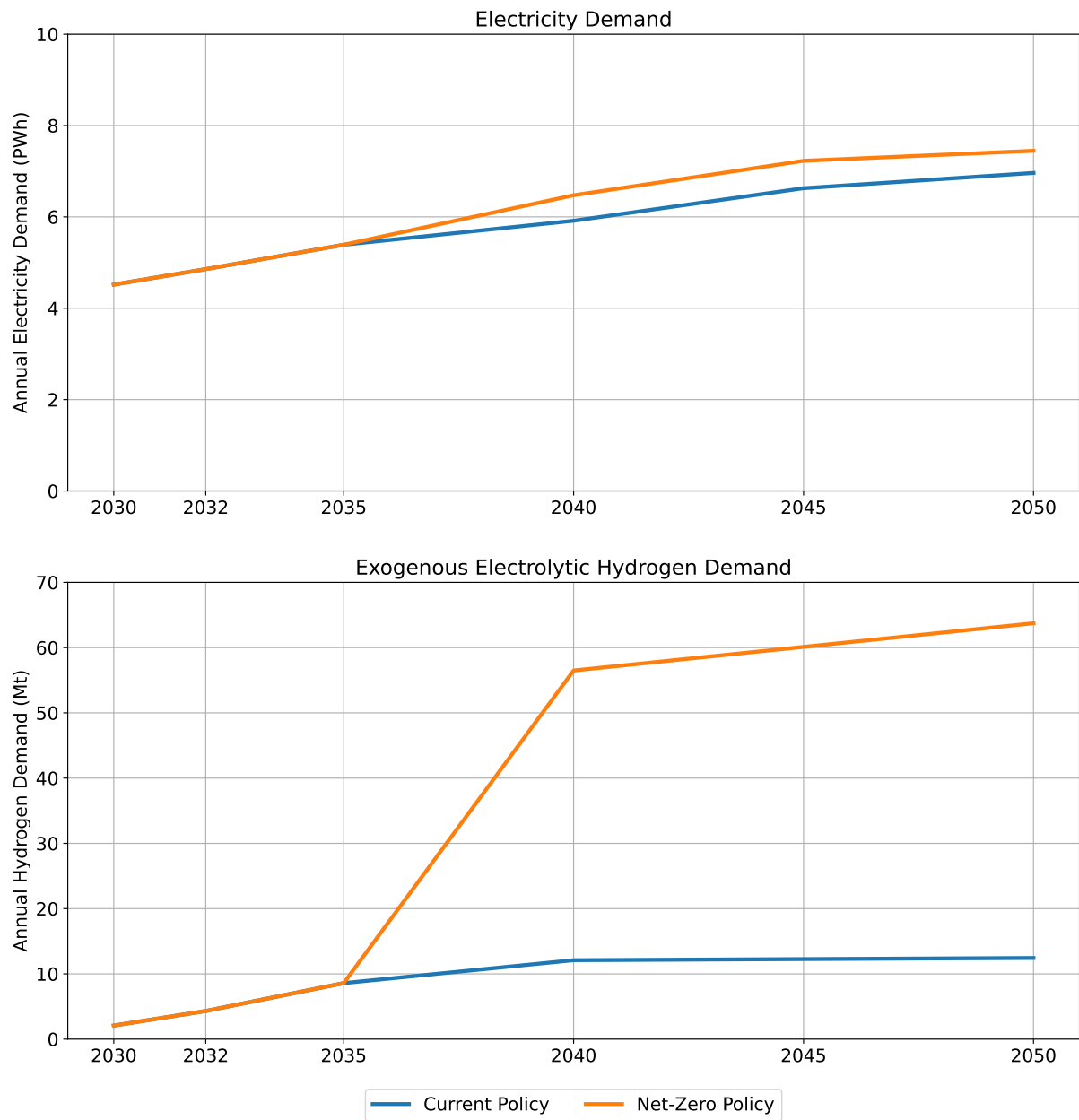


Figure S29: Electricity demand and exogenous electrolytic hydrogen demand assumptions, by year and scenario.

subsidy by 10% as well to reflect similar support for these resources. In the ‘Early Clean Firm Deployment Mandate’ case, we enforce minimum capacity requirements in the model for EGS, nuclear SMR, and Allam cycle technologies of 1250 MW in 2032 and 4450 MW in 2035, close to the maximum allowable growth rate for these technologies. In the ‘24/7 Carbon-Free Electricity Demand’ case, we require that a fixed percentage of electricity demand be met by local, newly-deployed carbon-free resources, defined here as wind, solar, hydrothermal, EGS, nuclear SMRs, Allam cycle gas, and storage charged using these resources. The participating percentage of demand is set at 2.5% in 2032, 5% in 2035, and rises by 5% in every planning period thereafter. This demand is additive to any demand for time-matched carbon-free electricity from hydrogen electrolyzers receiving 45¢ subsidies.

Supplementary References

1. Blackwell, D., Richards, M., Frone, Z., Batir, J., Ruzo, A., Dingwall, R., and Williams, M. (2011). Temperature-At-Depth Maps for the Conterminous U. S. and Geothermal Resource Estimates. *GRC Transactions* 31, 1545–1550.
2. Aljubran, M., and Horne, R. (2024). Thermal Earth model for the conterminous United States using an interpolative physics-informed graph neural network. *Geothermal Energy* 12. doi: <https://doi.org/10.1186/s40517-024-00304-7>.
3. Ricks, W., Voller, K., Galban, G., Norbeck, J.H., and Jenkins, J.D. (2024). The role of flexible geothermal power in decarbonized electricity systems. *Nature Energy*. doi: <https://doi.org/10.1038/s41560-023-01437-y>.
4. NREL. 2023 Annual Technology Baseline. Tech. Rep. National Renewable Energy Laboratory Golden, CO (2023).
5. Doe, T., and McLaren, R. (2016). Discrete Fracture Network Analysis of Controlling Factors for EGS Performance. In *Proceedings of the 41st Workshop on Geothermal Reservoir Engineering*. Stanford, CA.
6. US DOE. GeoVision. Tech. Rep. U.S. Department of Energy (DOE) (2019).
7. Mines, G. GETEM User Manual. Tech. Rep. INL/EXT-16-38751 Idaho National Laboratories Idaho Falls, ID (2016).
8. Ricks, W., and Jenkins, J. (2024). Pathways to national-scale adoption of enhanced geothermal power through experience-driven cost reductions: Supplementary Data. Zenodo. doi: [10.5281/zenodo.13357010](https://doi.org/10.5281/zenodo.13357010).
9. Williams, C., Reed, M., Mariner, R., DeAngelo, J., and Galanis, S. Assessment of Moderate- and High-Temperature Geothermal Resources of the United States. Tech. Rep. 2008-3082 U.S. Geological Survey (USGS) Menlo Park, CA (2008).
10. Allis, R., Gwynn, M., Hardwick, C., Hurlbut, W., and Moore, J. (2018). Thermal Characteristics of the FORGE site, Milford, Utah. *GRC Transactions* 42, 1011–1025.
11. The Future of Geothermal Energy. Tech. Rep. INL/EXT-06-11746 Idaho National Laboratory Idaho Falls, ID (2006).

12. Ricks, W., Norbeck, J., and Jenkins, J. (2022). The value of in-reservoir energy storage for flexible dispatch of geothermal power. *Applied Energy* 313, 118807. doi: <https://doi.org/10.1016/j.apenergy.2022.118807>.
13. Rutqvist, J., Pan, L., Spycher, N., Dobson, P., Zhou, Q., and Hu, M. (2020). Coupled Process Analysis of Flexible Geothermal Production from Steam- and Liquid-Dominated Systems: Impact on Wells. In *Proceedings of the 45th Workshop on Geothermal Reservoir Engineering*. Stanford, CA.
14. Rutqvist, J., Pan, L., Dobson, P., Zhou, Q., and Hu, M. (2021). Coupled Process Analysis of Flexible Geothermal Production from a Liquid-Dominated System: Impact on Wells. In *Proceedings of the World Geothermal Congress 2020+1*. Reykjavik, Iceland.
15. Norbeck, J., and Latimer, T.M. (2023). Commercial-Scale Demonstration of a First-of-a-Kind Enhanced Geothermal System. . Preprint, DOI: <https://doi.org/10.31223/X52X0B>.
16. Schivley, G., Welty, E., Patankar, N., Jacobson, A., Xu, Q., Manocha, A., Pecora, B., Bhandarkar, R., Jenkins, J.D., and Fripp, M. (2024). PowerGenome/PowerGenome: v0.6.3. Zenodo. doi: <https://doi.org/10.5281/zenodo.11194213>.
17. EIA. Annual Energy Outlook 2022. Tech. Rep. U. S. Energy Information Administration (EIA) Washington, DC (2022).
18. Viswanathan, V., Mongird, K., Franks, R., Li, X., Sprenkle, V., and Baxter, R. 2022 Grid Energy Storage Technology Cost and Performance Assessment. Tech. Rep. PNNL-33283 Pacific Northwest National Lab Richland, WA (2022).
19. Gagnon, P., Pham, A., and Cole, W. 2023 Standard Scenarios Report: A U.S. Electricity Sector Outlook. Tech. Rep. NREL/TP-6A40-87724 National Renewable Energy Laboratory Golden, CO (2024).
20. Jenkins, J.D., Farbes, J., and Jones, R. Climate Progress 2024: REPEAT Project's Annual U.S. Emissions Pathways Update. Tech. Rep. REPEAT Project (2024).
21. H.R.5376 (2022). Inflation Reduction Act. 117th Congress (2021-2022).